

## ABSTRACT

Title of Document: COMBINATORIAL DISCOVERY OF A MORPHOTROPIC PHASE BOUNDARY IN A LEAD-FREE PIEZOELECTRIC MATERIAL

Shigehiro Fujino, Doctor of Philosophy, 2008

Directed By: Professor Ichiro Takeuchi  
Department of Materials Science and Engineering

$\text{BiFeO}_3$  (BFO) is known to display rich and intricate multiferroic and chemical properties. It has a high switchable polarization and piezoelectric properties similar to  $\text{PbTiO}_3$ , but it also suffers from high coercive fields and high leakage currents. This has prompted investigations of doped-BFO as novel solid solutions which may emulate the performance of  $\text{PbZr}_{1-x}\text{Ti}_x\text{O}_3$  (PZT) in the composition range of  $0.48 < x < 0.52$ , where a morphotropic phase boundary (MPB) resides and displays substantially enhanced piezoelectric and ferroelectric properties. However neither an increase in electromechanical constants as a function of dopant concentration or domain structures indicative of a MPB piezoceramic had been reported in lead-free BFO-based systems prior to this work. There are some guidelines which predict the presence of MPBs, and one can explore novel compositions by systematically searching for similar structural transitions. Yet comprehensive mapping of compositions requires synthesis of an enormously large number of individual samples. We report on the discovery of a lead-free morphotropic (composition dependent, temperature independent) phase boundary with a simple perovskite structure. The combinatorial thin film strategy was used to

identify a rhombohedral to pseudo-orthorhombic structural transition which exhibits a ferroelectric to antiferroelectric transition at approximately  $\text{Bi}_{0.86}\text{Sm}_{0.14}\text{FeO}_3$ . At the morphotropic phase boundary, there is substantial enhancement in the dielectric properties. The piezoelectric coefficient of  $\text{Bi}_{0.86}\text{Sm}_{0.14}\text{FeO}_3$  film is comparable to that of  $\text{PbZr}_{0.52}\text{Ti}_{0.48}\text{O}_3$  thin film. The discovered compound is a strong candidate of a lead-free piezoelectric material.

**COMBINATORIAL DISCOVERY OF A MORPHOTROPIC PHASE  
BOUNDARY IN A LEAD-FREE PIEZOELECTRIC MATERIAL**

**By**

**Shigehiro Fujino**

**Dissertation submitted to the Faculty of the Graduate School of the  
University of Maryland, College Park, in partial fulfillment  
of the requirements for the degree of  
Doctor of philosophy  
2008**

**Advisory Committee:**

**Professor Ichiro Takeuchi, Chair and Advisor**

**Professor Manfred Wuttig, Advisor**

**Professor Lourdes G. Salamanca-Riba**

**Professor H. Dennis Drew**

**Professor Samel E. Lofland**

**© Copyright by  
Shigehiro Fujino  
2008**

## **Acknowledgements**

I would like to express my sincere gratitude to my advisor, Professor Ichiro Takeuchi, for giving me the opportunity to work on this challenging and exciting project. I benefited from all the discussions we had. It was his creative thoughts and suggestions that led the way for progress throughout my Ph.D study. His enthusiasm and collaborative spirit helped to create a great work environment.

The same gratitude goes to co-advisor Professor Manfred Wuttig. His amazingly broad knowledge was truly inspirational. I really appreciate both advisors tireless efforts to save my papers and presentations from my poor communication skills in English. If it were not for their patience, this research would not have been realized at Maryland.

Also, I would like to thank Dr. Makoto Murakami who has taught me pulsed laser deposition and XRD analysis. I am truly grateful for his valuable lessons.

I would like to thank Dr. V. Nagarajan and V. Anbusathaiah for measuring the ferroelectric properties of my samples using piezoforce microscopy.

I would also like to thank the other members of my committee, Professor Lourdes G. Salamanca-Riba, Professor Samel E. Lofland, and Professor H. Dennis Drew for their guidance. I would like to thank S.-H. Lim for his help with TEM analysis. Also, I am grateful Dr. Daisuke Kan. We had many fruitful discussions on complex oxide thin film materials.

I am deeply indebted to all of my past and present group members. In particular, Christian Long, Dr. Jason. R. Hattrick-Simpers, and Dwight Hunter for helping me with the initial screening of my poor English before submitting materials

to my advisors. Also, I would like to thank Dr. Kao-Shuo Chang and Hiroyuki Ohguchi for their leadership in winning the 2004 softball tournament at the University of Maryland. GO, GO, COSMIC!!!

Finally, I would like to thank my family for their love and support. I own everything I achieved to them. This thesis is dedicated to them.

# Table of Contents

Acknowledgements.....	ii
List of Tables .....	vi
List of Figures.....	vii
CHAPTER 1. INTRODUCTION.....	1
1-1 Motivation .....	1
1-2 Ferroelectric and antiferroelectric phenomena in perovskite crystals	5
1-3 Piezoelectricity .....	8
1-4 Morphotropic phase boundaries (MPB's).....	12
1-5 Multiferroic BiFeO <sub>3</sub> .....	14
1-6 Combinatorial strategy: thin film composition spread technique.....	17
CHAPTER 2. CHARACTERIZATION OF THIN FILMS .....	20
2-1 Structural characterization of the film .....	21
2-1-1 X-ray diffraction (XRD) .....	21
2-1-2 Transmission electron microscope (TEM) .....	23
2-2 Electrical characterization of the thin film.....	23
2-2-1 Schematic structure of sample for electrical measurement.....	23
2-2-3 Piezoelectric force microscope (PFM) .....	25
2-2-4 Dielectric constant and loss factor (tan $\delta$ ).....	26
CHAPTER 3. FERROELECTRIC PROPERTIES OF MULTIPHASE Bi-Fe-O THIN FILMS .....	27
3-1: Introduction .....	28
3-2: Experimental procedure .....	29
3-3: Multiple phase formation in Bi-Fe-O thin films as a function of oxygen deposition pressure. ....	29
3-4-1: TEM .....	32
3-4-2: Reciprocal space maps.....	34
3-5: Electric properties of red and yellow BiFeO <sub>3</sub> thin films. ....	36
3-5-1: Leakage current density as a function of applied electric field. ...	36
3-5-2: Polarization electric field hysteresis loops (P-E) .....	39
3-6: Conclusion.....	43

CHAPTER 4. COMBINATORIAL DISCOVERY OF A MORPHOTROPIC PHASE BOUNDARY IN $\text{Bi}_{1-x}(\text{RE})_x\text{FeO}_3$ (RE : RARE EARTH) THIN FILM COMPOSITION SPREADS .....	44
4-1 Introduction .....	45
4-2: Experimental procedure .....	45
4-3: Microstructure of $\text{Bi}_{1-x}\text{Sm}_x\text{FeO}_3$ thin films .....	46
4-3-1: XRD of BSFO composition spread thin film. ....	46
4-3-2: TEM of BSFO at MPB composition .....	49
4-5: Ferroelectric and antiferroelectric in $\text{Bi}_{1-x}\text{Sm}_x\text{FeO}_3$ thin films. ....	51
4-5-1: P-E loops of BSFO thin films .....	51
4-5-2: Dielectric constant as a function Sm content.....	54
4-5-3: Piezoelectric coefficient $d_{33}$ as a function of Sm content.....	54
4-5-4: $d_{33}$ loops for $\text{BiFeO}_3$ and $\text{Bi}_{0.86}\text{Sm}_{0.14}\text{FeO}_3$ .....	57
4-5-5: Rayleigh analysis of the measured out-of-plane piezoresponse for the MPB composition ( $\text{Bi}_{0.86}\text{Sm}_{0.14}\text{FeO}_3$ ).....	57
4-5-6: Capacitance as a function of DC bias-voltage (C-V) curve of antiferroelectric part of thin film. ....	61
4-5-7: $d_{33}$ loop for antiferroelectric part of thin film. ....	61
4-6. Other possible MPBs in other rare earth doped (La, Gd, Dy, and Lu) $\text{BiFeO}_3$ .....	65
4-7: Conclusion.....	71
 CHAPTER 5. CONCLUSIONS AND FUTURE WORK.....	 72
5-1. Conclusions .....	72
5-2. Possibility applications of MPB BSFO and future work.....	75
5-2-1. New multiferroic spintronic device.....	76
 BIBLIOGRAPHY .....	 78

## **List of Tables**

Table 1. Restriction of Hazardous Substances (RoHS).....	2
Table 2. Ferroelectric and antiferroelectric materials in perovskite structure .....	6
Table 3. Piezoelectric properties of representative piezoelectric materials .....	11

## List of Figures

Figure 1-1. Replacing lead containing electrical/electronic materials.....	3
Figure 1-2. Application of PZT materials.....	4
Figure 1-3. Ferroelectric (a) and Antiferroelectric (b) .....	6
Figure 1-4. Perovskite structure $ABO_3$ .....	7
Figure 1-5. Piezoelectric phenomena... ..	10
Figure 1-6. A single layer piezoelectric actuator (a) and Displacement as a function of electric field (b).....	11
Figure 1-7. $PbZr_{1-x}Ti_xO_3$ phase diagram [Ref.11] .....	12
Figure 1-8. Schematic structure of $BiFeO_3$ [Ref 23] .....	15
Figure 1-9. Polarization of single crystal (a) [Ref. 28] and thin film (b) [Ref. 4].....	16
Figure 1-10. A photograph of a discrete combinatorial library [Ref. 33] .....	17
Figure 1-11. Schematic of pulsed laser deposition (PLD) .....	19
Figure 1-13. Schematic of composition spread fabrication technique .....	19
Figure 2-1. Schematic of the initial screening techniques for a composition spread film .....	20
Figure 2-2. Scannig x-ray diffractometer used for phase identification composition spread films. (D8 discover with GADDS by Bruker-AXS) [Ref 35] .....	21
Figure 2-3. Diffraction patterns of conventional ( $\theta$ - $2\theta$ ) (a) and two dimensional (partial picture) XRD (b) .....	22
Figure 2-4 Schematic of sample structure for electrical characterization .....	23
Figure 2-5 A typical ferroelectric polarization – electric field (P-E) hysterysis loop .....	24

Figure 2-6 Schematic of the piezoelectric force microscope (a) PFM set up, (b) PFM image (qualitative measurement), and piezoelectric coefficient $d_{33}$ as a function of an electric field (quantitative measurement) .....	25
Figure 2-7 Parallel plate capacitance .....	26
Figure 3-1 Schematic of multiphase formation in $\text{BiFeO}_3$ as a function of oxygen pressure during the deposition.....	31
Figure 3-2 TEM bright field cross-sectional images from BFO films deposited at oxygen pressure of a) 35 mTorr (yellow) and b) 20 mTorr (red). The films were fabricated on $\text{SrRuO}_3$ buffered (50 nm) $\text{SrTiO}_3$ (001) substrates. c) SAD pattern and d) plan-view image from red-BFO indicating existence of the $\text{Fe}_2\text{O}_3$ in the films .....	33
Figure 3-3 Reciprocal space maps of pure $\text{BiFeO}_3$ and nanocomposite $\text{BiFeO}_3 - \text{Fe}_2\text{O}_3$ films grown on $\text{SrTiO}_3$ (001) substrate.....	35
Figure 3-4 Leakage current density as a function of applied electric field on nanocomposite $\text{BiFeO}_3 - \text{Fe}_2\text{O}_3$ (20 mTorr) and pure $\text{BiFeO}_3$ (35 mTorr) thin films .....	38
Figure 3-5 Polarization electric field (P-E) hysteresis loops of pure BFO and BFO - $\text{Fe}_2\text{O}_3$ composite films measured at 5 kHz and at room temperature.....	41
Figure 3-6 Remnant polarization ( $P_r$ ) as function of applied electric field in pure BFO and nanocomposite BFO- $\text{Fe}_2\text{O}_3$ thin films measured at a frequency of 1 kHz and at room temperature .....	42

Figure 4-1 X-ray diffraction and PFM mapping of $\text{Bi}_{1-x}\text{Sm}_x\text{FeO}_3$ composition spread (a) $\theta$ - $2\theta$ scan from $43^\circ$ to $48^\circ$ across a composition spread (6 mm long) on [001] $\text{SrTiO}_3$ and initial piezoforce microscopy (PFM) mapping of piezo response from the BSFO composition spread (b).....	47
Figure 4-2 Two-dimensional diffraction images ( $Q_z$ - $Q_x$ ) taken from $x = 0$ to $x = 0.3$ in $\text{Bi}_{1-x}\text{Sm}_x\text{FeO}_3$ composition spread .....	48
Figure 4-3 High resolution plan-view transmission electron microscopy image of the composition at the morphotropic phase boundary (MPB, $x = 0.14$ ). .....	50
Figure 4-4 Polarization hysteresis loops for three selected compositions.....	53
Figure 4-5 Dielectric constant ( $\epsilon_{33}$ ) and $\tan \delta$ measured at 10 kHz (zero-bias).....	55
Figure 4-6 High-field piezoelectric coefficient ( $d_{33}$ ) and coercive field ( $E_c$ ) determined from the piezoelectric hysteresis loops measured as a function of composition. ....	56
Figure 4-7 Piezoelectric properties of $\text{Bi}_{1-x}\text{Sm}_x\text{FeO}_3$ (a) $d_{33}$ loops for $\text{BiFeO}_3$ and $\text{Bi}_{0.86}\text{Sm}_{0.14}\text{FeO}_3$ .....	58
Figure 4-8 Rayleigh analysis measurements for the MPB composition sample.....	59
Figure 4-9 Capacitance vs. electric field for the antiferroelectric (AFE) composition at $\text{Bi}_{0.84}\text{Sm}_{0.16}\text{FeO}_3$ . ....	62
Figure 4-10 Antiferroelectric $d_{33}$ loop is observed for $\text{Bi}_{0.84}\text{Sm}_{0.16}\text{FeO}_3$ . ....	63
Figure 4-11 Calculation of cell volume vs total energy for antiferromagnetic $\text{BiFeO}_3$ in different possible structural arrangements [Ref. 78].....	66

Figure 4-12 Strategy scheme of search for other possible MPBs for other rare earth doped BiFeO <sub>3</sub> strategic.....	67
Figure 4-13 Out-of-plane lattice constant mapped by scanning XRD for other rare earth doped BiFeO <sub>3</sub> composition spreads Bi <sub>1-x</sub> RE <sub>x</sub> FeO <sub>3</sub> .....	68
Figure 4-14 P-E loops from other rare earth doped BiFeO <sub>3</sub> measured from other compositions from respective composition spreads. ....	69
Figure 5-1 Schematic of multiferroic spintronic device structure.....	75
Figure 5-2 Approached to FeRAM device.....	76

# CHAPTER 1. INTRODUCTION

## 1-1 Motivation

The dangers of lead (Pb) are well recognized, and laws are being introduced internationally to curb its use. An urgent need for lead free electrical/electronic materials arose when the European Union (EU) introduced legislation for use of Pb free materials in 2003. The EU had investigated how much waste an average person creates in his/her lifetime as a result of using electrical products such as refrigerators, microwave ovens, TVs, PCs, cell phones, etc. This number was estimated to be an astounding 7,500 pounds which triggered the 2002 EU Waste Electrical and Electronic Equipment Directive (WEEE), which included the hazardous substance directive (RoHS).<sup>1</sup> Both became the law a year later. This law holds the manufacturers responsible for the disposal of WEEE: the companies are required to establish an infrastructure for collecting WEEE, in such a way that "users of electrical and electronic equipment from private households should have the possibility of returning WEEE at least free of charge." In addition, the companies are forced to use the collected waste in an ecologically-friendly manner, either by ecological disposal or by its reuse. Furthermore, the RoHS is strictly prohibiting the use of the six materials listed in Table 1 in the manufacturing of electronic equipment. These hazardous materials had to be eliminated from all new electrical products manufactured since July 1, 2006. Naturally, this waste disposal and recycling effort can be reduced if new lead free electronic materials which replace these materials can be developed. This need then motivates the present research.

**Table 1. Restriction of Hazardous Substances (RoHS)**

- 1. Lead : Pb**
- 2. Mercury : Hg**
- 3. Cadmium : Cd**
- 4. Hexavalent chromium (chromium xxx or Cr6+)**
- 5. Polybrominated biphenyls (PBB)**
- 6. Polybrominated diphenyl ether (PBDE)**

Hazardous substances were to be completely eliminated from electronic devices by July 1, 2006 as mandated by Restriction of Hazardous Substances (RoHS) in Europe. Pb containing components have been used in many types of electrical devices. For example, tin/lead solders with lead concentrations between 30% and 95% by weight are commercially available and are widely used. The greater the tin concentration, the greater the solder's tensile and shear strength. However, in order to decrease melting temperature of the solders, lead is used. Another class of lead containing materials is used to produce ceramic capacitors which constitute the most used passive devices in electronic circuits. The compositions  $\text{PbMg}_{1/3}\text{Nb}_{2/3}\text{O}_3$  (PMN) and  $\text{PbTiO}_3$  (PTO), called relaxor materials, have particularly large dielectric constants and are thus preferred as they permit miniaturization of the capacitors. Fortunately, the research community has found alternative materials for both solder and capacitors before the July 1, 2006 deadline. The Pb-based solder materials are replaced by SnCu, SnAg, and SnZnBi,<sup>2</sup> while  $\text{BaTiO}_3$  is the most popular material for the replacement of Pb-based relaxors in the passive device market now (Figure1-1).

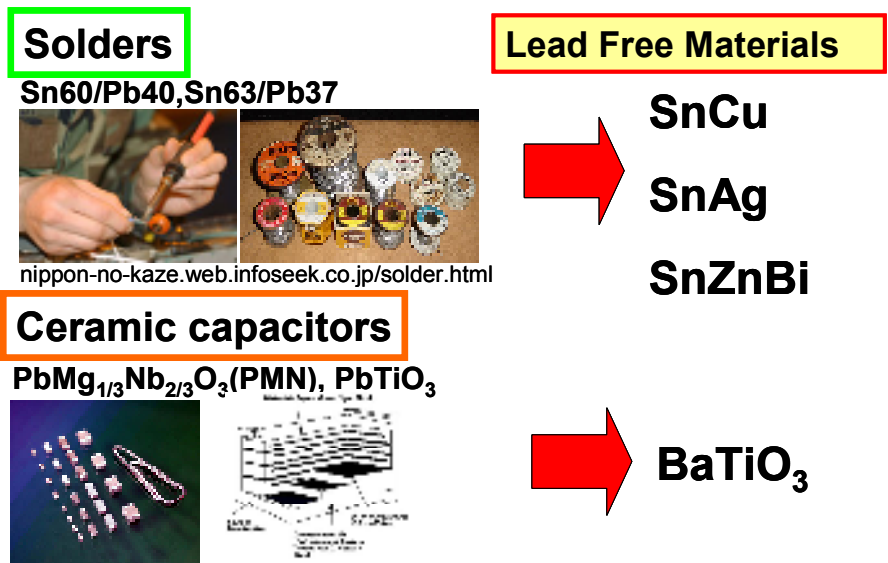


Figure 1-1. Replacing lead containing electrical/electronic materials

An exception to this trend is lead zirconium titanate,  $\text{PbZr}_x\text{Ti}_{1-x}\text{O}_3$  (PZT), which contains over 40% Pb concentration and for which no commercial replacement has been found yet. PZT is widely used to fabricate ultrasound transducers, actuators, as well as ferroelectric random access memory (FeRAM) chips (Figure1-2). Because of its large polarization and piezoelectric coefficient, it is widely used for a variety of electronic devices. The part of the motivation of this thesis is directed towards exploration of new lead free piezoelectric material(s).

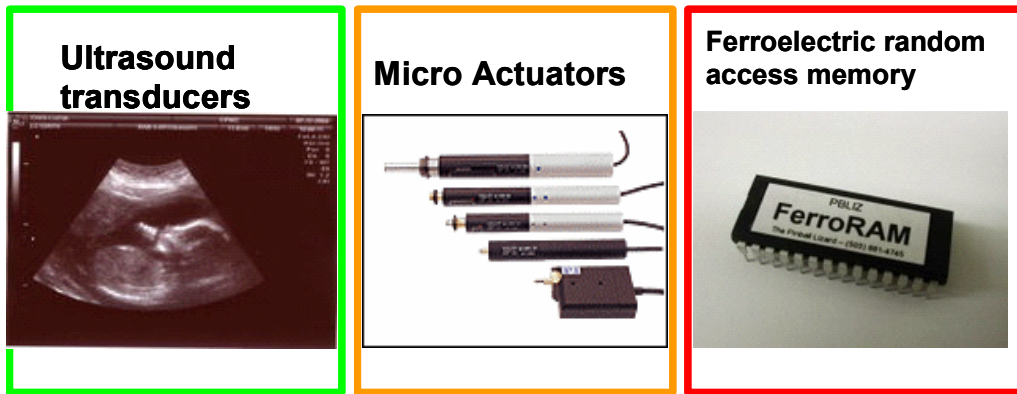


Figure 1-2. Examples of application of PZT materials

## **1-2 Ferroelectric and antiferroelectric phenomena in perovskite crystals**

Ferroelectric (FE) crystals exhibit electric dipole moments even in the absence of an external electric field but only below a characteristic temperature called the Curie temperature ( $T_c$ ). This polarization can be reoriented or reversed fully or in part by applying an electric field. The complete reversal of the spontaneous polarization is called “switching”. The non-polar phase above  $T_c$  is known as the paraelectric phase. The direction of the spontaneous polarization conforms to the crystal symmetry of the material.<sup>3</sup> When a ferroelectric crystal is distorted, there is a structure it can take where the original unit cell is doubled and as a result, there is alternating antiparallel order of the polarization. Such a crystal is called antiferroelectric (AFE).<sup>4</sup> The energy difference between the undistorted and distorted structures could be small and hence some antiferroelectrics can be forced into a ferroelectric state by applying a strong electric field<sup>5, 6</sup> (Figure 1-3). Table 2 lists some typical ferroelectric and antiferroelectric perovskites. The occurrence of ferroelectricity and antiferroelectricity in perovskites indicates that this structure can be relatively easily distorted.<sup>7</sup> The general perovskite compound has an  $ABO_3$  structure, where the A site-ion is singly, doubly or triply positively charged while the ionization state of the B-ion is +5, +4, or +3 (Figure 1-4).<sup>8</sup>

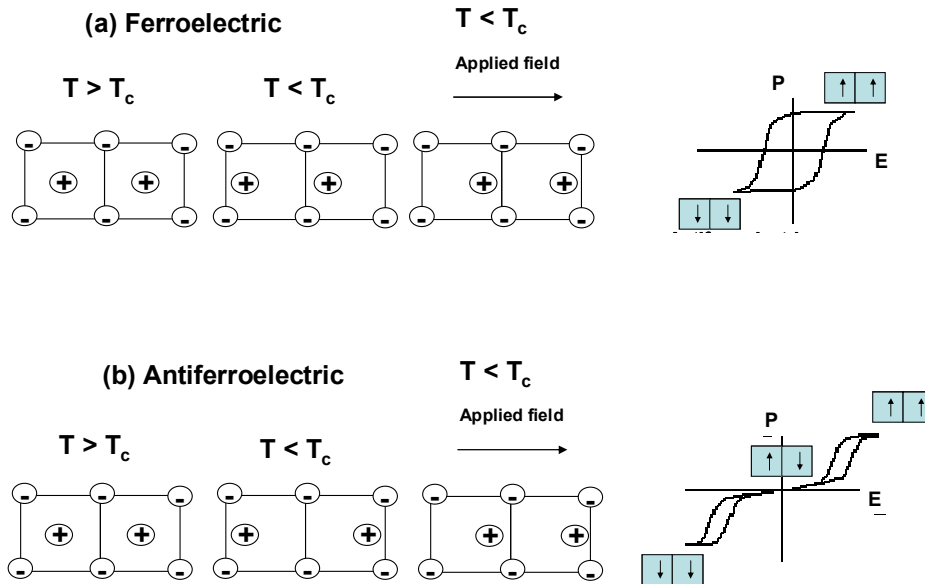
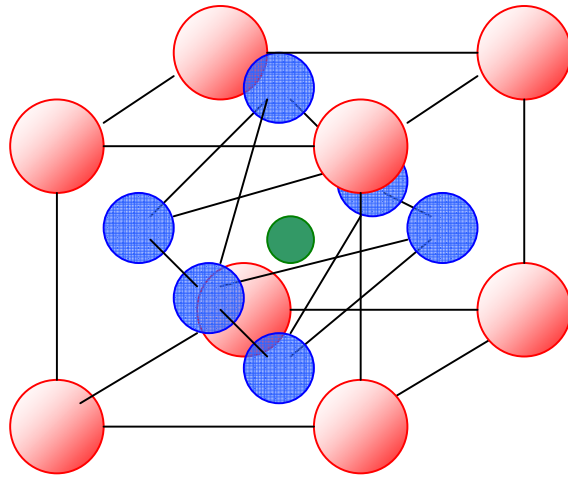


Figure 1-3. Ferroelectricity (a) and antiferroelectricity (b)

Table 2. Ferroelectric and antiferroelectric materials in perovskite structure

Perovskite structure	Composition	Curie temperature ( $T_c$ ) in Celsius
Ferroelectric	$\text{BaTiO}_3$	130
	$\text{PbTiO}_3$	463
	$\text{BiFeO}_3$	790
Antiferroelectric	$\text{PbZrO}_3$	233
	$\text{PbHfO}_3$	215
	$\text{NaNbO}_3$	520



-  **A-site: +1 to +3**
-  **B-site: +5 to +3**
-  **Oxygen: -2**

Figure 1-4. Perovskite structure  $ABO_3$  and the valance state of respective ions

### 1-3 Piezoelectricity

All ferroelectric materials are piezoelectric. However, not all piezoelectric materials are ferroelectric. Piezoelectric materials develop electric charges at surfaces when they are mechanically deformed. This is the direct piezoelectric effect. Conversely, when an external electric field is applied to piezoelectric materials they mechanically deform. This is the converse piezoelectric effect. These effects are schematically depicted in Figure 1-5. The most widely used piezoelectric material is lead zirconate titanate:  $\text{PbZr}_x\text{Ti}_{1-x}\text{O}_3$  (PZT). Since PZT has a large electromechanical coupling coefficient at composition ratio approximately Zr/Ti: 50/50.<sup>9</sup> This small composition region is called a morphotropic phase boundary (MPB). More details on the MPB will be presented in Section 1-4. PZT is widely in the used electronic device. The device application of PZT include:

- \* Piezoelectrics for ultrasound, medical imaging, and actuators
- \* Non-volatile memory devices
- \* Capacitors
- \* Oscillators and filters
- \* Light deflectors

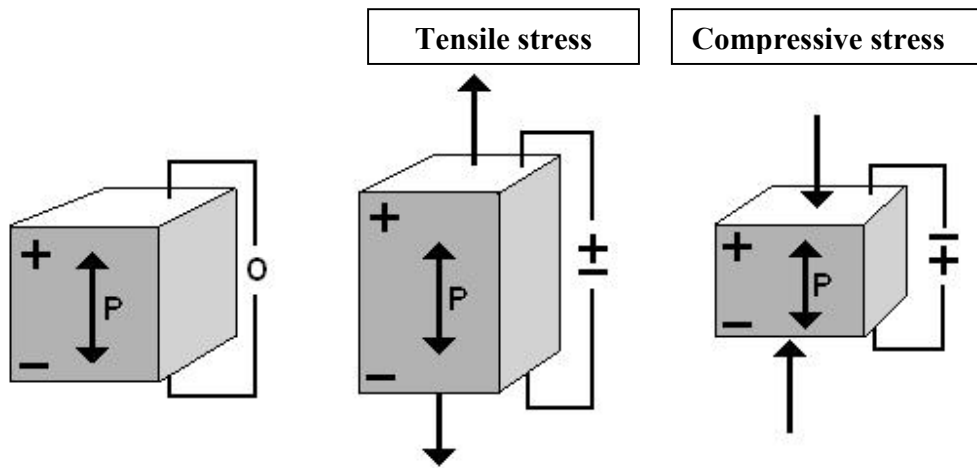
The most dominant use of PZT has been in actuators and transducers. Figure 1- 6 shows a single layer piezoelectric actuator. The piezoelectric actuator is primarily a function of applied electric field (E), the length (L) of the actuator, the forces applied to it and the piezoelectric coefficient  $d_{ij}$  of the material used. The change in length (D and

L) of an unloaded single-layer piezoelectric actuator can be estimated by the following equation:

$$\Delta L = S \cdot L_0 \approx \pm E \cdot d_{ij} \cdot L_0 \quad (\text{Eq-1})$$

where, S is strain,  $L_0$  = sample length [m], E = electric field strength [V/m], and  $d_{ij}$  = piezoelectric coefficient of the material [m/V] respectively. Table 3 lists piezoelectric coefficient  $d_{33}$  of representative piezoelectric materials<sup>10, 15</sup>

**(a) direct piezoelectric effect**



**(b) converse piezoelectric effect**

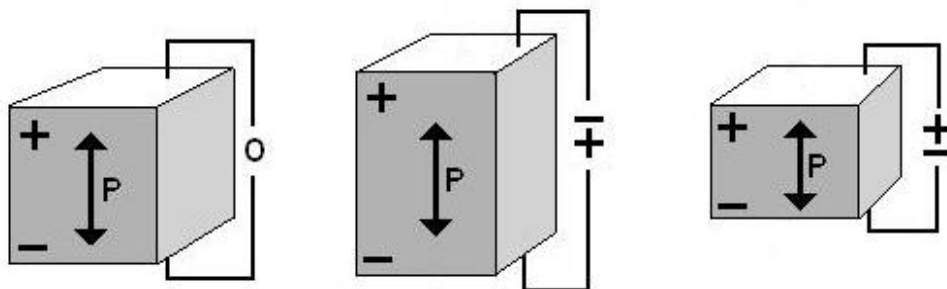


Figure1-5. Piezoelectric phenomena. Direct piezoelectric effect (a) and converse piezoelectric effect (b)

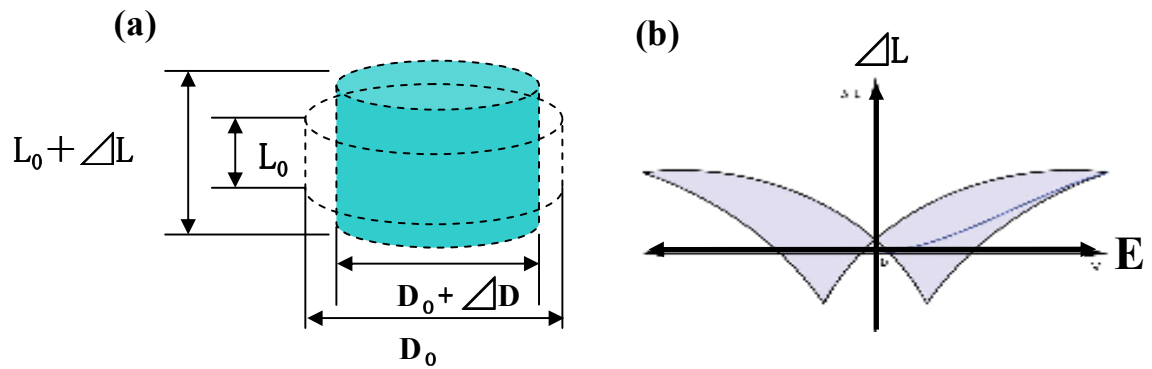


Figure1-6. A single layer piezoelectric actuator (a) and Displacement as a function of electric field (b).

Table 3. Piezoelectric properties of representative piezoelectric materials [Ref 10, 15]

Compounds	Piezoelectric constant: $d_{33}$	$T_c$ (°C)
<b>PbZr<sub>0.52</sub>Ti<sub>0.48</sub>O<sub>3</sub> (bulk)</b>	<b>289</b>	<b>328</b>
<b>PbZr<sub>0.52</sub>Ti<sub>0.48</sub>O<sub>3</sub> (thin film: 200nm)</b>	<b>160</b>	
<b>BaTiO<sub>3</sub></b>	<b>190</b>	<b>120</b>
<b>(Pb,Sm)TiO<sub>3</sub></b>	<b>65</b>	<b>355</b>
<b>Quarts</b>	<b>2.3</b>	
<b>Polyvinylidene Fluoride (PVDF)</b>	<b>33</b>	

## 1-4 Morphotropic phase boundaries (MPB's)

Figure 1-7 shows the well-known PZT phase diagram. This phase diagram has a morphotropic phase boundary (MPB).<sup>11</sup> The MPB characterizes a temperature independent and composition dependent structural phase transition from a rhombohedral (space group R3m) to a tetragonal (space group P4mm) phase or vice versa. The phase boundary is almost a vertical straight line. Hence, the transition is practically temperature independent. At the MPB, PZT possesses large electromechanical coupling properties. The exact origin of the large piezo-response near the MPB is still under debate.<sup>12, 13</sup> As we search for a Pb free replacement for PZT, we hope to find a replacement materials which displays a MPB as well.

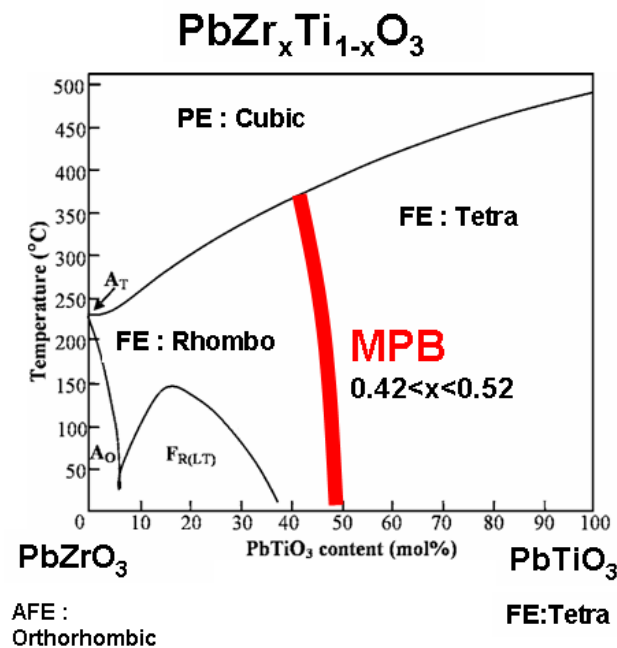


Figure 1-7.  $\text{PbZr}_{1-x}\text{Ti}_x\text{O}_3$  phase diagram [Ref. 11]

In 2003, J. Wang *et al.*<sup>14</sup> reported that epitaxially strained BiFeO<sub>3</sub> (BFO) thin films grown with a SrRuO<sub>3</sub> (SRO) buffer layer on SrTiO<sub>3</sub> (100) substrates showed a large polarization of 60  $\mu\text{C}/\text{cm}^2$  at room temperature. This perovskite is lead free and ecologically friendly. The value of the polarization of BFO is much higher than that of the currently popular PZT thin films.<sup>15</sup> However, BFO films have a large coercive field ( $E_c$ ) and, a lower piezoelectric coefficient ( $d_{33}$ ) in comparison to PZT.<sup>11, 12, 16, 17</sup> Chemical doping and substitution is often used as a tool to modify, enhance properties of ferroelectric materials. We decided to use BFO as basis of our new system and perform systematic chemical substitution studies to identify compositions with enhanced ferroelectric and piezoelectric properties.

## 1-5 Multiferroic BiFeO<sub>3</sub>

We chose multiferroic BiFeO<sub>3</sub> as a basis of our dopant investigation. Multiferroic materials where multiple ferroic properties coexist are attractive for novel device applications such as inexpensive, ultra-sensitive magnetometers and bi-ferroic memory elements where spontaneous polarization and magnetization are coupled.<sup>18, 19</sup> BiFeO<sub>3</sub> (BFO) is a single phase multiferroic material. It has a rhombohedrally distorted structure that shows ferroelectricity ( $T_c \approx 850$  °C) and a G-type antiferromagnetism ( $T_N \sim 370$ °C) at room temperature.<sup>20, 21</sup> The ferroelectricity of BFO is caused by the active lone pairs on the Bi ions, which takes place large displacements of the Bi and O ions along the [111] direction as shown Figure 1-8.<sup>22</sup>

It is often difficult to synthesize single phase BFO without impurity phases because Bi is a volatile element, and secondary phases such as Bi<sub>2</sub>Fe<sub>4</sub>O<sub>9</sub><sup>23</sup> and Fe<sub>2</sub>O<sub>3</sub><sup>24</sup> have been reported. BFO also has a high leakage current problem since insufficient oxygen pressure can cause valence fluctuation of Fe ions (+3 to +2) and oxygen vacancies.<sup>25, 26</sup> Teague *et al.*<sup>27</sup> had reported that a bulk BFO single crystal showed a small spontaneous polarization of  $3.5 \mu\text{C}/\text{cm}^2$  along the [111] direction with an applied electric field of 55 kV/cm at 77K in an unsaturated polarization hysteresis loop (Figure 1-9 (a)). Recently, Wang *et al.*<sup>4</sup> reported that strained BFO films grown with a SrRuO<sub>3</sub> (SRO) buffer layer on SrTiO<sub>3</sub> (100) substrates showed a polarization of  $60 \mu\text{C}/\text{cm}^2$  at electric field of 500 kV/cm at room temperature (Figure 1-9 (b)). The high polarization was reported to be due to the heteroepitaxial strain. However, recent reports indicate that the epitaxial strain is not necessary for high polarization in BFO thin films<sup>28, 29, 30</sup>

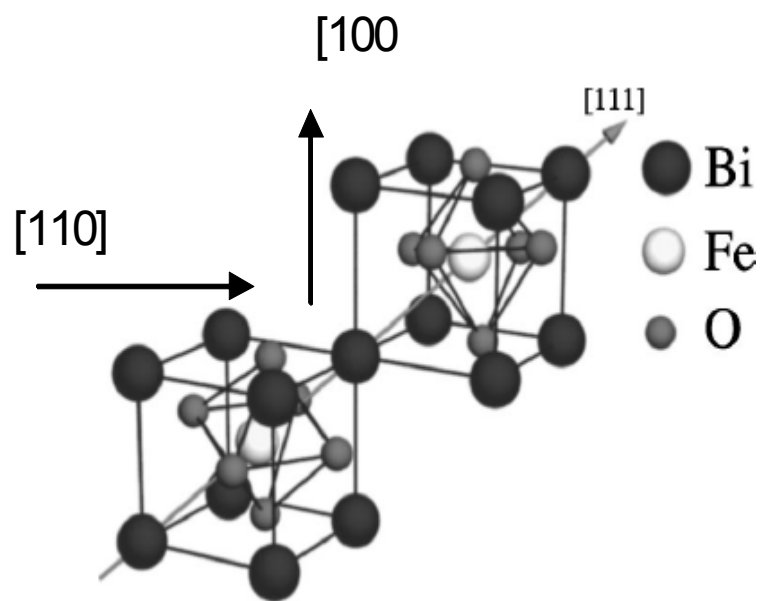
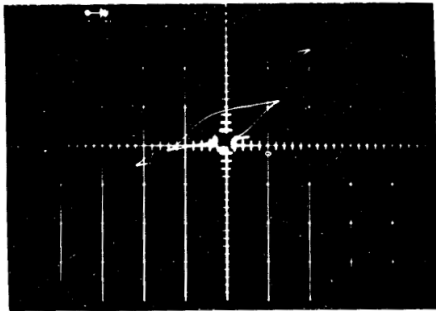


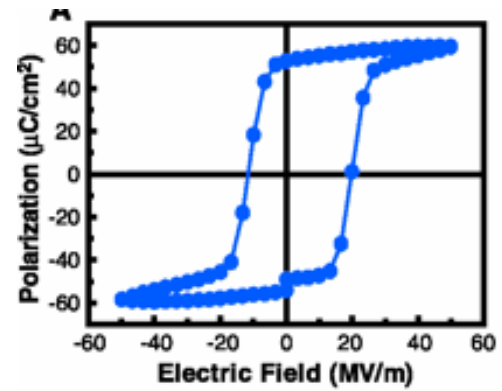
Figure 1- 8. Schematic structure of BiFeO<sub>3</sub> [Ref 23]

Single crystal



$P = 3.5 \mu\text{C}/\text{cm}^2$  at 77K

Thin film



$P = 60 \mu\text{C}/\text{cm}^2$  at RT.

Figure 1- 9. Polarization of single crystal (a) [Ref. 28] and thin film (b) [Ref. 4]

## 1-6 Combinatorial strategy: thin film composition spread technique

In order to explore doped BFO system, we have applied the combinatorial thin film approach. The combinatorial technique was first introduced in the pharmaceutical industry in 1980s.<sup>31</sup> The idea behind the combinatorial approach is to fabricate and characterize many different materials in one run, instead of one at a time. As an example, Figure 1- 10 shows a discrete type combinatorial library used to search for new luminescent materials.<sup>32</sup> Each square spot has a different composition. The combinatorial approach can be used to rapidly screen a wide range of compositional landscapes in individual experiments.

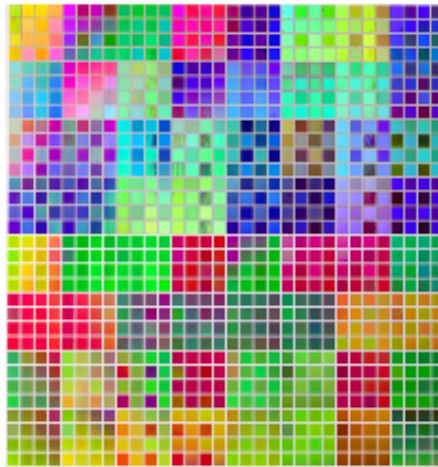


Figure 1-10. A photograph of a discrete combinatorial library. [Ref. 33]

The combinatorial approach to materials science as a field has made much progress in the last ten years. One can now implement controlled synthesis of nano meter thickness layer by layer structure using pulsed laser deposition (PLD) as shown Figure 1-11. Moving shadow masks and a multi targets system can be implemented to create

composition variation.<sup>33</sup> This method enables fabrication of thin film composition spreads which allows us to track the change in crystal structures and physical properties as a continuous function of composition. PLD is a widely used physical vapor deposition technique for thin film research. PLD uses a high power pulsed laser beam to ablate a ceramic or a metal target of desired composition. The target material is vaporized and deposited on a substrate. This process operates in ultra high vacuum from  $10^{-10}$  to  $10^{-7}$  Torr. Reactive gas such as oxygen or nitrogen is introduced into the chamber during deposition. Figure 1-12 shows the schematic of the composition spread fabrication using PLD in detail. In order to fabricate the thin film composition spread, two ceramic targets of two distinct compositions, A and B are ablated in an alternating manner with a KrF excimer laser ( $\lambda = 248$  nm) with a typical fluence of  $2 \text{ J/cm}^2$  using a carousel targets system over the substrate during the deposition (Fig.1-12(a))<sup>34</sup>. Linear compositional gradient across the spreads such as  $\text{Ba}_{1-x}\text{Sr}_x\text{TiO}_3$  or  $\text{Bi}_{1-x}\text{Sm}_x\text{FeO}_3$  is formed by moving a shadow mask system placed over the substrate back and forth during the deposition. The typical distance between the shutter plane and the substrates is  $300 \mu\text{m}$ . The motion of the shutter is synchronized with the firing of the laser in such a way so that for each deposition, a thickness gradient “wedge” is created on the chip. Deposition at an elevated temperature allows us to synthesize epitaxial films in-situ on lattice matched substrates. In order to ensure alloy-like intermixing of A and B at the atomic level, less than a unit cell ( $\approx 0.4 \text{ nm}$ ) is deposited for each set of A/B deposition at any position on the spread chip (Fig 1-12 (b)). In a spread sample, the resulting composition of the spread varies continuously from pure A at one end to pure B at the other end which has a 6 mm of composition spread region (Fig 1- 12 (c)). A and B are

often isostructural compounds so that we can use this approach to explore the effect of continuous substitution.

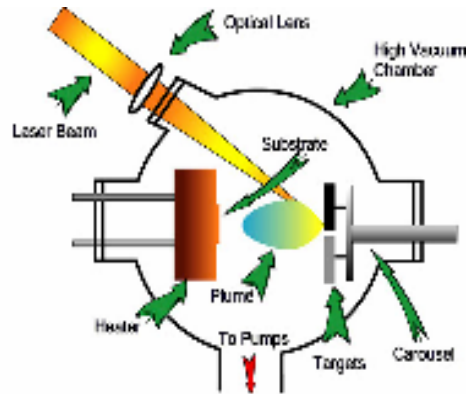


Figure 1-11. Schematic of a pulsed laser deposition (PLD) chamber

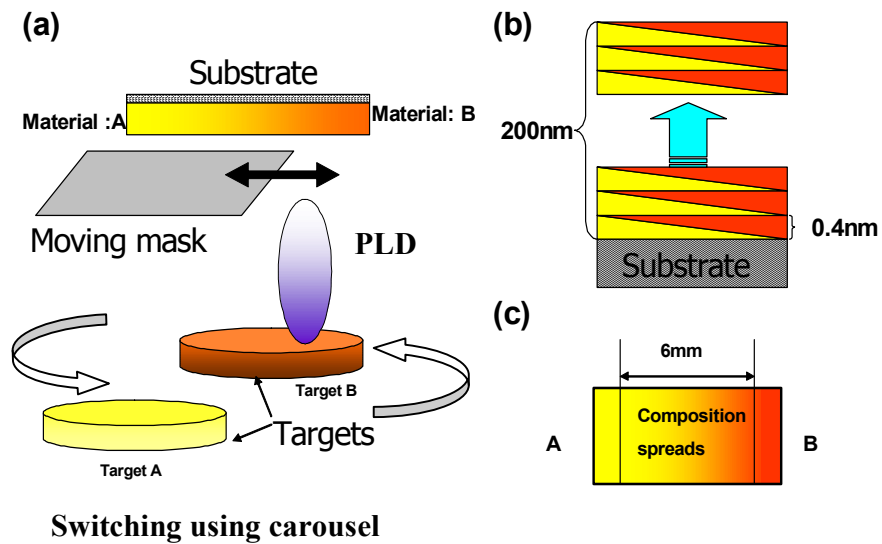


Figure 1-12. Schematic of composition spread fabrication technique

## CHAPTER 2. CHARACTERIZATION OF THIN FILMS

Pulsed laser deposition (PLD) with moving shutters and a multi targets system has been used to fabricate composition spread films (Chapter 1, Section 1-5). In this chapter, I introduce the characterization techniques used to determine the film properties. The process of initial screening is often crucial in the combinatorial strategy since it allows us to quickly determine which regions are of interest and require detailed screening and characterization. For the initial characterization of the piezoelectric properties, we used piezo-response force microscopy (PFM), and x-ray microdiffraction was used to study the crystal structures. The ferroelectric properties of the films were measured using a commercially available Radiant Technology (Precision LC) system to determine. A HP4275A LCR meter was used for dielectric constant and loss factor measurements. The detailed crystal structure of the films was analyzed using a JEOL 2100 F field emission transmission electron microscope (TEM).

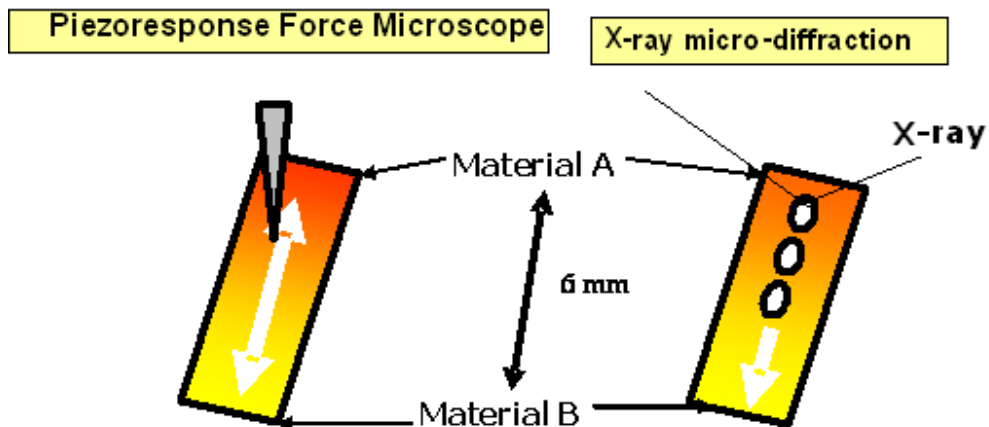


Figure 2-1. Schematic of the initial screening techniques for a composition spread film.

## 2-1 Structural characterization of the film

### 2-1-1 X-ray diffraction (XRD)

X-ray diffraction (XRD) is one of the most popular and powerful technique to investigate the crystal structure of a material. The Bragg condition for constructive interference is  $n\lambda = 2d \sin\theta$ ; where  $\lambda$  is the x-ray wavelength,  $n$  is an integer,  $d$  is the crystal plane spacing, and  $\theta$  is the x-ray incident angle. This forms the basis for the interpretation of XRD results. In this thesis work, a D8 Discover with GADDS by Bruker-AXS with a two-dimensional (2D) detector (diameter 11.5 cm) was used for measurement at temperatures between room temperature and 400 °C.<sup>8,35</sup> This system features an XYZ stage permitting automated point by point measurements across the composition spread films.

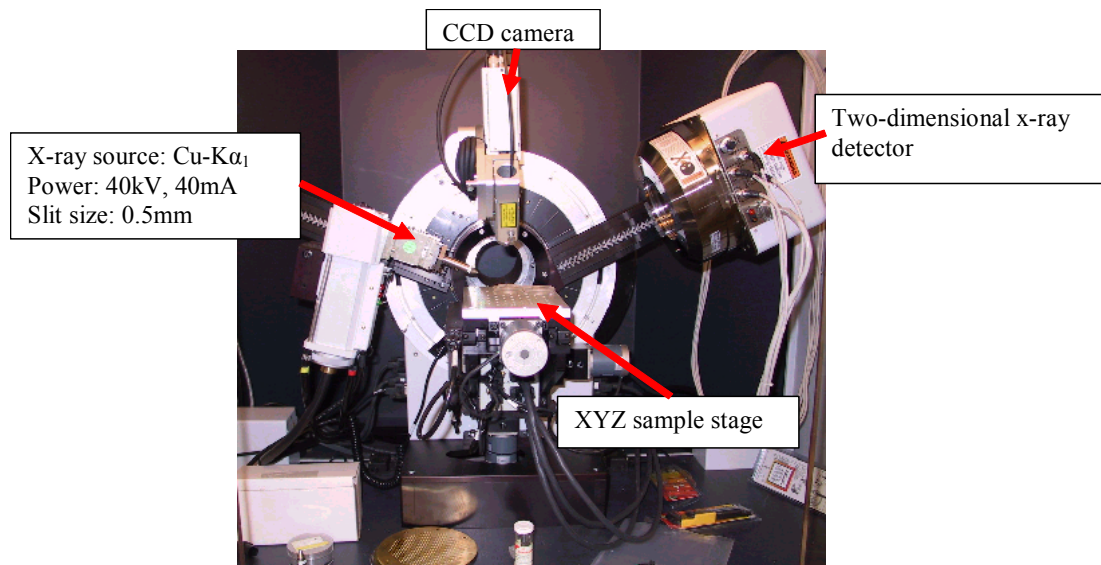


Figure 2-2. Scannig x-ray diffractometer used for phase identification composition spread films. (D8 discover with GADDS by Bruker-AXS) [Ref 35]

Figure 2-3 shows (a) the conventional diffraction pattern and (b) a 2D-XRD image of an epitaxial thin film on a substrate from the same sample. From the peak position, we can calculate the out of plane lattice constant of the films. The 2D-XRD image displays spots in the center which are associated with the film and the substrate out of plane direction. The vertical direction of the image corresponds to the in-plane direction of the film. The 2D diffraction pattern contains more information than the  $\theta$ - $2\theta$  diffraction, and it can be used to obtain information such as phase identification, percent crystallinity, particle size, texture, and stress.<sup>36</sup>

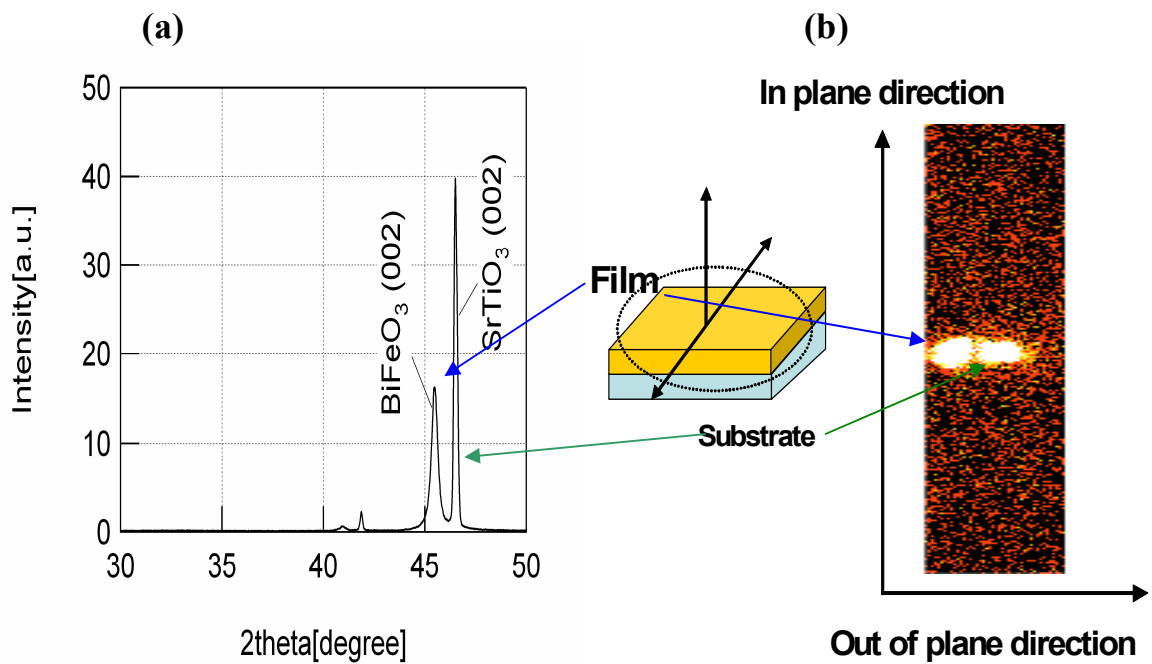


Figure 2-3. Diffraction patterns of conventional ( $\theta$ - $2\theta$ ) (a) and two dimensional (partial picture) XRD (b).

### 2-1-2 Transmission electron microscope (TEM)

A JEOL 2100 F field emission transmission electron microscope operating at 200 kV was used for microstructural characterization. Lattice parameters were calculated from small area electron diffraction patterns. To investigate defects and interface condition in the films, we used high-resolution TEM images. For details on TEM analyses of the materials in this thesis, the reader is referred to the References 37, and 38.

## 2-2 Electrical characterization of the thin film

### 2-2-1 Schematic structure of sample for electrical measurement

For electrical characterization, an epitaxial SrRuO<sub>3</sub> layer (50 nm) was used as the bottom electrode, and a sputter-deposited top Pd layer (100 nm) was photolithographically patterned into 50 μm capacitor dots. This device configuration (shown in Figure 2-4) is used for measurement of polarization, dielectric constant, and the piezoelectric coefficient.

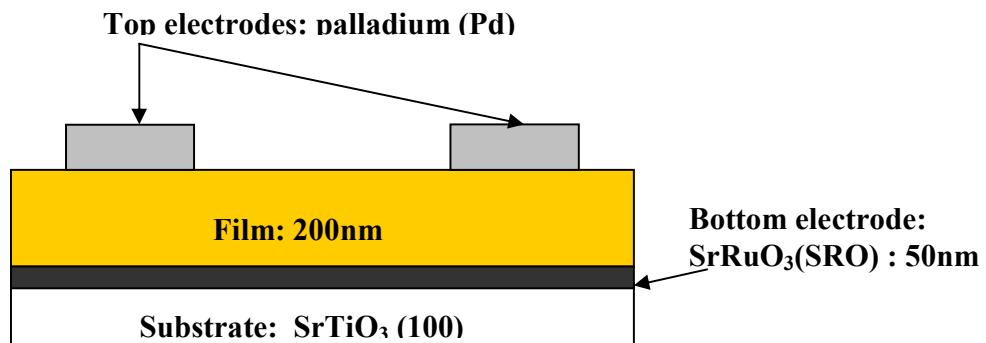


Figure 2-4. Schematic of sample structure for electrical characterization

### 2-2-2 Polarization hysteresis loop (P-E loop)

Ferroelectric hysteresis loops were measured using a Radiant Technology: Precision LC at of the measurement frequency of 5 kHz. Figure 2-5 shows an example of a polarization hysteresis loop quantified by the parameters such as saturation polarization ( $P_s$ ), remnant polarization ( $P_r$ ) and coercive field ( $E_c$ ) as shown in the figure. The  $P_s$  is extrapolated from the saturated polarization point. The  $P_r$  is the remaining polarization value when the electric field is reduced to zero. In order to remove the overall polarization of the crystal, one has to apply an electric field in the opposite direction. The value of the field required to decrease polarization to zero is called the  $E_c$ .<sup>39, 40</sup>

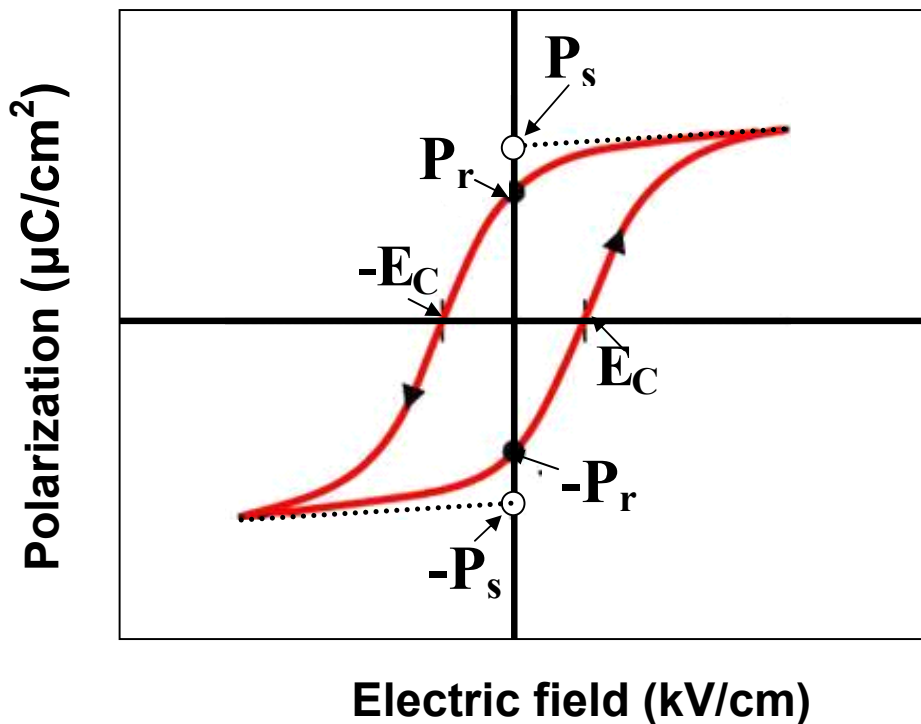


Figure 2-5. A typical ferroelectric polarization – electric field (P-E) hysteresis loop.

### 2-2-3 Piezoelectric force microscope (PFM)

A PFM consists of a conventional atomic force microscope. A PFM is fitted with a Pt-Ir coated conductive cantilever tip, a photodiode, a laser source and external lock-in amplifiers to track the piezoelectric response of the ferroelectric materials under investigation. Figure 2-6 shows the schematic of a PFM. Quantitative PFM was performed on the Pd/(Bi,Sm)FeO<sub>3</sub>/SRO/STO structures using contact mode tips. The measurement frequency was 7 kHz. In this thesis, PFM is used to obtain  $d_{33}$  hysteresis loops ( Figure 2-6 (b)). The details on the calibration of the PFM technique are given in Reference 27.

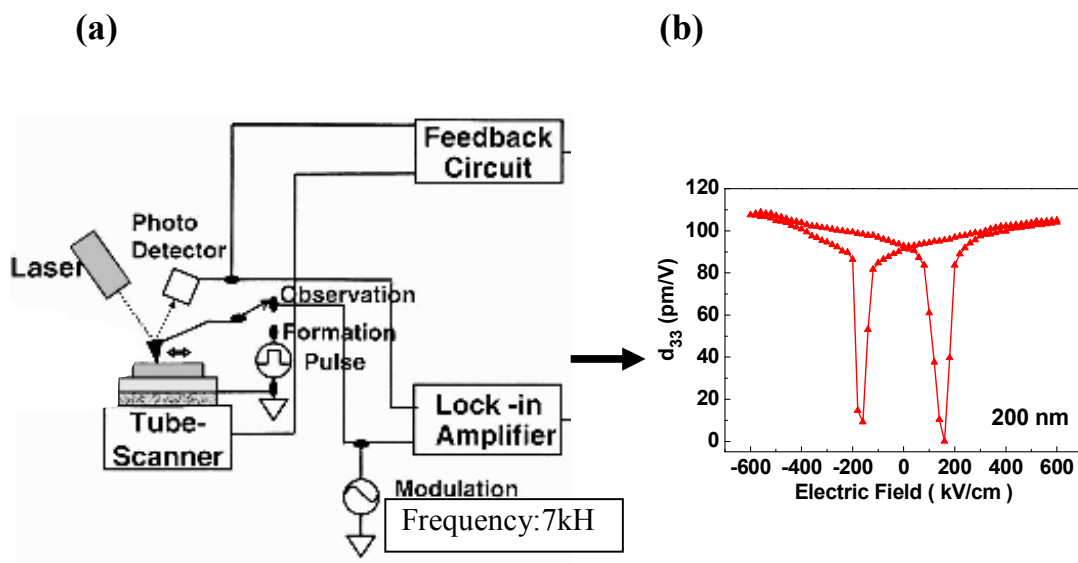


Figure 2-6. Schematic of the piezoelectric force microscopy (a) PFM set up, and (b) piezoelectric coefficient  $d_{33}$  as a function of an electric field (quantitative  $d_{33}$  hysteresis loop measurement)

#### 2-2-4 Dielectric constant and loss factor ( $\tan \delta$ )

An HP 4275A LCR meter was used for capacitance measurements using a modulation voltage of 100 mV at 10 kHz. The dielectric constant was calculated from the equation 2 :

$$C = \frac{\epsilon_0 \epsilon_r A}{t} \quad (\text{Eq - 2})$$

Here, C is the capacitance,  $\epsilon_0$  the permittivity of vacuum,  $\epsilon_r$  the relative dielectric constant of the sample material, and t is the thickness as shown in Figure 2-7.<sup>41</sup>

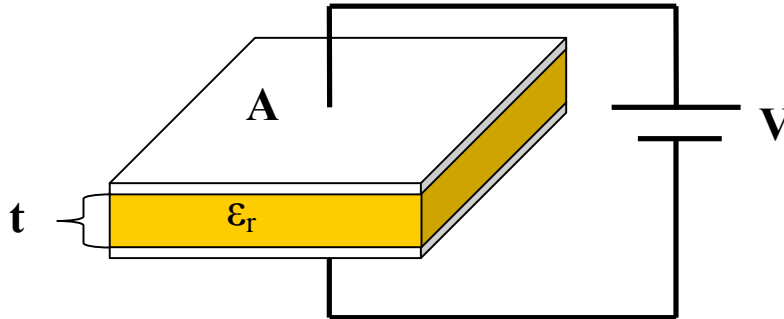


Figure 2-7. Parallel plate capacitor

## **CHAPTER 3. FERROELECTRIC PROPERTIES OF MULTIPHASE Bi-Fe-O THIN FILMS**

To find the basis for a new system containing a MPB, we initially looked into the Bi based perovskites  $\text{BiFeO}_3$ ,<sup>42</sup>  $\text{BiCrO}_3$ ,<sup>43</sup> and  $\text{BiMnO}_3$ .<sup>44</sup> In particular, we chose the BFO system as a basis of our detailed dopant studying because of its good ferroelectric properties and interesting magnetic properties at room temperature.<sup>21, 22, 23</sup> In general, we found that due to the volatile nature of A-site, Bi is a very volatile element. Therefore, it is difficult to obtain high quality films. Therefore, we concentrated first on determining the optimum deposition conditions for these Bi-based materials.

In this chapter, we discuss the ferroelectric properties of pure BFO films and nanocomposite films of BFO and  $\text{Fe}_2\text{O}_3$ , which form as a result of Bi off-stoichiometry induced decomposition. The formations of dominant phases were controlled by varying the oxygen deposition pressure. The microstructure of BFO thin films was investigated using TEM and various XRD techniques including the reciprocal space mapping using a Bruker GADDS D8.

### 3-1: Introduction

BiFeO<sub>3</sub> (BFO) is known to display rich and intricate multiferroic and chemical properties.<sup>19</sup> It has a high switchable polarization and piezoelectric properties similar to PbTiO<sub>3</sub>, but it also suffers from the high coercive field and the high leakage current. We investigated the ferroelectric properties of multiphase Bi-Fe-O thin films grown under varying oxygen deposition pressures. The dominant phases formed in the films continuously change from a mixture of BiFeO<sub>3</sub> with Bi<sub>2</sub>O<sub>3</sub> to a mixture of BiFeO<sub>3</sub> with Fe<sub>2</sub>O<sub>3</sub> as the pressure is varied. X-ray diffraction and transmission electron microscopy revealed that epitaxial BiFeO<sub>3</sub> and Fe<sub>2</sub>O<sub>3</sub> were grown when the deposition pressure was  $\approx 20$  mTorr, and the BiFeO<sub>3</sub> grains were completely relaxed thereby eliminating epitaxial strains. At room temperature, a high switchable polarization ( $60 \mu\text{C}/\text{cm}^2$ ) and a low leakage current density ( $\approx 1 \times 10^{-4} \text{ A}/\text{cm}^2$  at  $250 \text{ kV}/\text{cm}$ ) were observed in the BiFeO<sub>3</sub>-Fe<sub>2</sub>O<sub>3</sub> film. In this chapter, we report on the dielectric and ferroelectric properties of pure BFO films and nanocomposite films of BFO and Fe<sub>2</sub>O<sub>3</sub>. The nanocomposite films consisting of BFO and Fe<sub>2</sub>O<sub>3</sub> were found to be fully relaxed and showed a well developed ferroelectric polarization loop at room temperature.

### **3-2: Experimental procedure**

In order to fabricate BFO thin films by pulsed laser deposition,  $\text{Bi}_{1.1}\text{FeO}_3$  target was ablated with a KrF excimer laser ( $\lambda = 248 \text{ nm}$ ) using a typical fluence of  $2 \text{ J/cm}^2$ . The oxygen pressure during deposition was varied in the range of  $10^{-4} - 10^{-1} \text{ Torr}$ . The substrate temperature was fixed at  $600 \text{ }^\circ\text{C}$ . The typical deposition rate was  $5 \text{ nm/min}$ , and  $\text{SrTiO}_3$  (STO) (001) substrates were used. TEM images and selected area diffraction (SAD) patterns of the films were obtained at an accelerating voltage of  $200 \text{ keV}$ .

### **3-3: Multiple phase formation in Bi-Fe-O thin films as a function of oxygen deposition pressure.**

In an earlier work by our group, we had reported on the magnetic properties of multiphase BFO thin films deposited at different oxygen pressures.<sup>43</sup> It was found that Bi evaporated from the films during the deposition, and  $\alpha$ - and  $\gamma$ -  $\text{Fe}_2\text{O}_3$  segregated from BFO. BFO and  $\text{Fe}_2\text{O}_3$  were found to grow epitaxially together at low oxygen pressures. This multiple phase formation process in BFO as a function of oxygen pressure during the deposition is summarized in Fig. 3-1:

Epitaxial single phase BFO films with the (001) orientation were obtained at oxygen pressures higher than  $1 \times 10^{-3} \text{ Torr}$ , and the volume fraction of the pure BFO phase increases as the pressure is increased. The  $\text{Fe}_2\text{O}_3$  phase was formed at oxygen pressure less than  $5 \times 10^{-3} \text{ Torr}$ . In the x-ray diffraction patterns of these films, the intensity of the peaks associated with  $\text{Fe}_2\text{O}_3$  increases as the oxygen pressure decreases.

A pure single phase BFO phase was obtained between  $5 \times 10^{-3}$  and  $5 \times 10^{-2}$  Torr. There are also noticeable differences in the color of the samples. The samples were red for oxygen partial pressure between  $5 \times 10^{-3}$  and  $2.5 \times 10^{-2}$  Torr, and yellow for oxygen pressure between  $2.5 \times 10^{-2}$  and  $5 \times 10^{-2}$  Torr. The natural color of BFO, which has a band gap of 2.5 eV<sup>45</sup> is yellow. It is believed that the red color originates from the Fe<sub>2</sub>O<sub>3</sub> phase because the color of a pure Fe<sub>2</sub>O<sub>3</sub> thin film is red.<sup>6</sup> Above 50 mTorr, we observed segregation of a Bi<sub>2</sub>O<sub>3</sub> phase in BFO thin films.<sup>46</sup> The transition of the dominant phase in the film changes from Fe<sub>2</sub>O<sub>3</sub> + BiFeO<sub>3</sub> to BiFeO<sub>3</sub> + Bi<sub>2</sub>O<sub>3</sub>. As the deposition oxygen pressure was decreased, the Bi content in the films decreased.

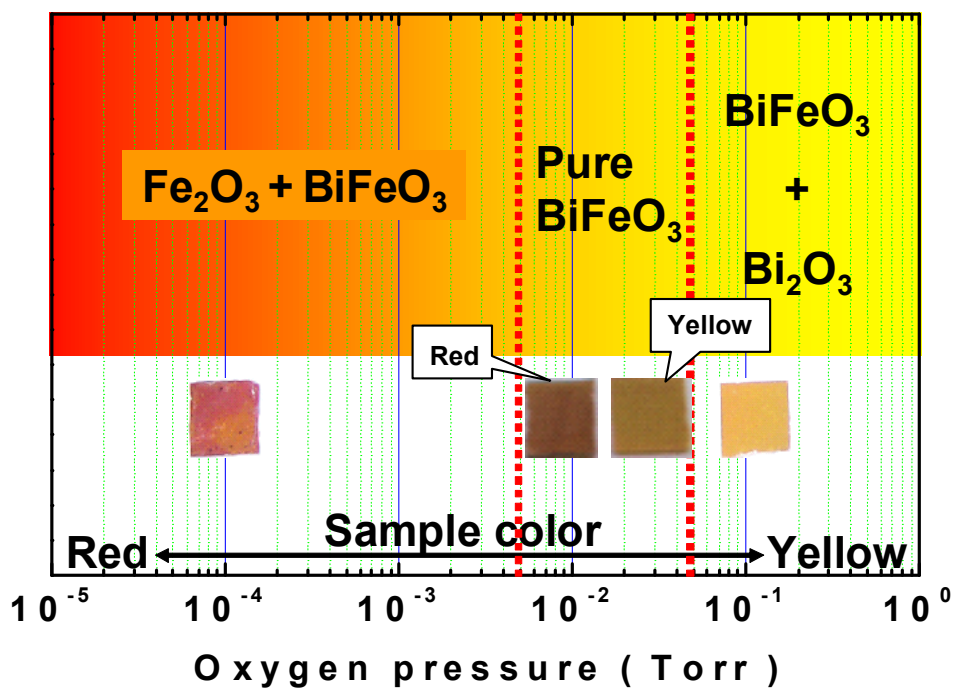


Figure 3-1. Schematic of multiphase formation in BiFeO<sub>3</sub> as a function of oxygen pressure during the deposition. The sample color changes from yellow to red as the pressure is decreased.

### 3-4: Microstructure of red and yellow BiFeO<sub>3</sub> thin films.

#### 3-4-1: TEM

Figure 3-2 shows cross-sectional TEM images of BFO samples deposited at an oxygen pressure of (a) 35 mTorr (sample color: yellow) and (b) 20 mTorr (sample color: red) thin films. Pure single phase BFO was observed in the films grown at 35 mTorr, while the Fe<sub>2</sub>O<sub>3</sub> phase was observed in the red-BFO film grown at oxygen deposition pressure of 20 mTorr. From the cross-sectional image in Figure 3- 2 (b) and the plan-view image in Fig. 2(d), we see that the red-BFO film grew epitaxially together with nano-sized (50 – 100 nm)  $\alpha$ -Fe<sub>2</sub>O<sub>3</sub> grains that nucleated at the SRO buffer or in the surface region of the film during deposition. From the diffraction pattern in Figure 3-2 (c), we obtained the following preferred in-plane epitaxial relations between BiFeO<sub>3</sub> and  $\alpha$ -Fe<sub>2</sub>O<sub>3</sub>;  $[100]_{\text{BiFeO}_3} // [102]_{\alpha}$ , and  $[010]_{\text{BiFeO}_3} // [1\bar{1}2]_{\alpha}$ , which are in good agreement with our previous results.<sup>6</sup> These results confirm that the red color of the films originates from the presence of the Fe<sub>2</sub>O<sub>3</sub> phase.

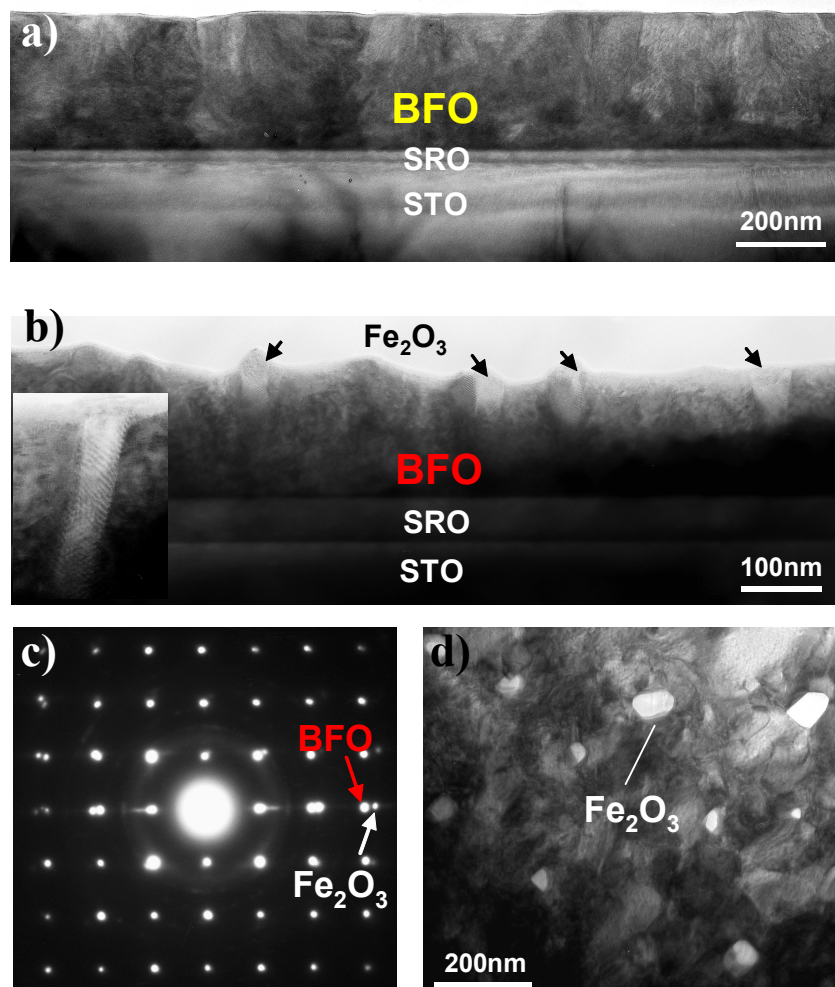


Figure 3-2. TEM bright field cross-sectional images from BFO films deposited at oxygen pressure of (a) 35 mTorr (yellow) and (b) 20 mTorr (red). The films were fabricated on SrRuO<sub>3</sub> buffered (50 nm) SrTiO<sub>3</sub> (001) substrates. (c) SAD pattern and (d) plan-view image from red-BFO indicating existence of the Fe<sub>2</sub>O<sub>3</sub> in the films.

### 3-4-2: Reciprocal space maps

To investigate the strain state evolution in the films, x-ray reciprocal space maps of the films and the substrates were measured. Figure 3-3 shows the reciprocal space maps of the (103) reflections of pure BFO and the BFO-Fe<sub>2</sub>O<sub>3</sub> nanocomposite thin films on STO (100) substrates. We found that the BFO crystals of the nanocomposite BFO films were fully relaxed, while the pure BFO films were completely strained by the STO substrate. The observed lattice parameters of the BFO phase in pure BFO and the nanocomposite BFO are  $a= 3.905 \text{ \AA}$ ,  $c= 4.030 \text{ \AA}$ , with  $c/a = 1.03$  and  $a= 3.948 \text{ \AA}$ ,  $c= 3.990 \text{ \AA}$ , with  $c/a = 1.01$  respectively. In another study, we have recently observed that the local formation of Fe<sub>2</sub>O<sub>3</sub> in the BFO films acts as a stress accommodating mechanism in BFO<sup>47</sup>. This is consistent with the present observation that the BFO component of the nanocomposite structure is stress relaxed.

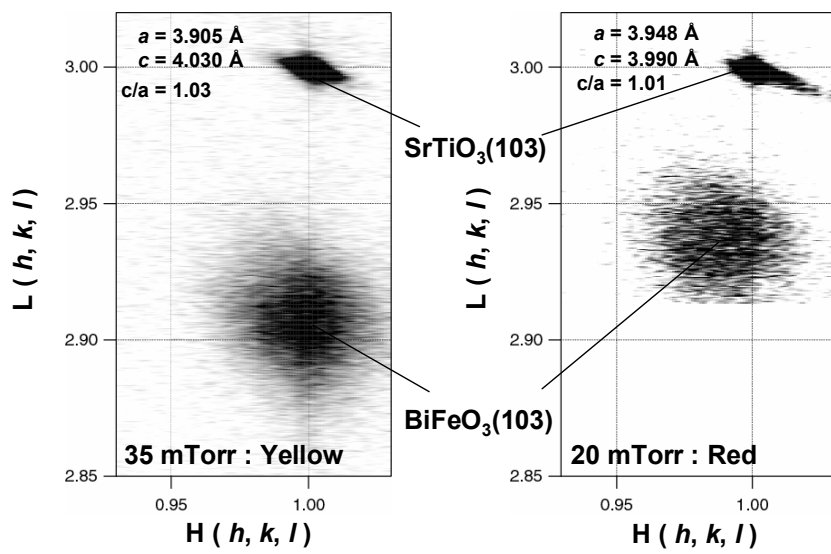


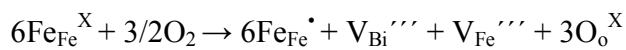
Figure 3-3. Reciprocal space maps of pure  $\text{BiFeO}_3$  and nanocomposite  $\text{BiFeO}_3 - \text{Fe}_2\text{O}_3$  films grown on  $\text{SrTiO}_3 (001)$  substrate. The red film is fully relaxed.

### 3-5: Electric properties of red and yellow BiFeO<sub>3</sub> thin films.

#### 3-5-1: Leakage current density as a function of applied electric field.

Generally, it is difficult to prepare oxide materials without oxygen vacancies. It is known that the electrical conductivity in BFO is related to the deviation of oxygen stoichiometry, which gives rise to valence fluctuation of Fe ions from +3 to +2.<sup>48, 49</sup>

Figure 3-4 plots the leakage current density as a function of applied electric field in the BFO-Fe<sub>2</sub>O<sub>3</sub> nanocomposite and pure BFO films. The leakage current density of the nanocomposite film ( $1 \times 10^{-4}$  A /cm<sup>2</sup>) is approximately two orders of magnitude smaller than that of the pure BFO film at an applied field of 250 kV/cm. Qi *et al.*<sup>7</sup> reported that the current density of Ti<sup>+4</sup> doped BFO films is three orders lower than that of non doped BFO at applied fields of 100 kV/cm or less. However, their films did not show a saturated polarization loop at room temperature. Dho *et al.*<sup>50</sup> had reported that BFO films grown with low oxygen deposition pressure and high deposition growth showed good saturated polarization loops at room temperature and the leakage current density of film was approximately  $1 \times 10^{-4}$  A/cm<sup>2</sup> at an applied field of 500 kV/cm. They proposed a cation vacancy model by creating a Fe<sup>+4</sup> valance state for explaining, a defect equation (Kroger - Vink notation) is:



where  $\text{Fe}_{\text{Fe}}^{\text{X}}$  is a 3+ Fe ion,  $\text{Fe}_{\text{Fe}}^{\bullet}$  is a 4+ Fe ion,  $\text{V}_{\text{Bi}}^{\prime\prime\prime}$  and  $\text{V}_{\text{Fe}}^{\prime\prime\prime}$  are cation vacancies, and  $3\text{O}_{\text{O}}^{\text{X}}$  is a divalent oxygen ion. The Fe<sup>4+</sup> can eliminate the cation vacancies during deposition.

X-ray photoelectron-spectroscopy (not shown) of our pure BFO films indicates

that  $\text{Fe}^{+3}$  is the only valence state in the films. The results are consistent with those reported by Eerenstein, *et al.*<sup>28</sup>

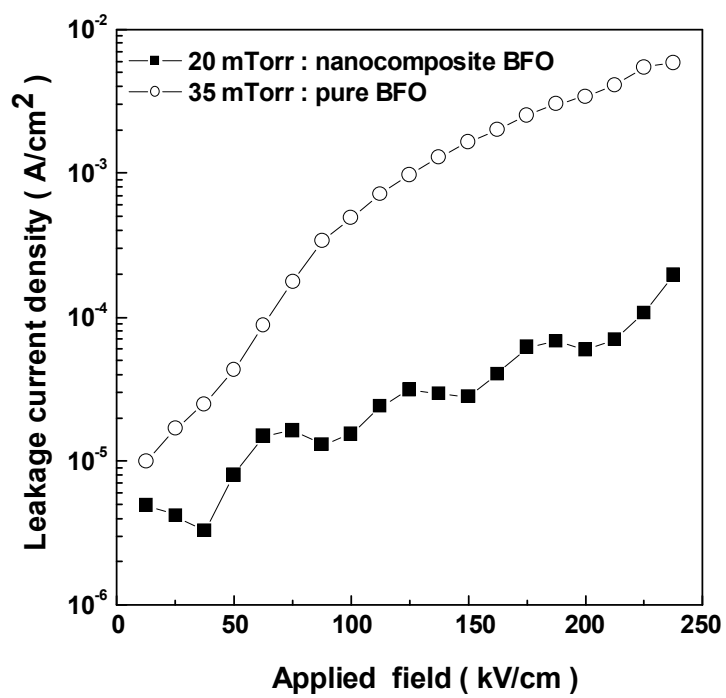


Figure 3-4. Leakage current density as a function of applied electric field for nanocomposite  $\text{BiFeO}_3 - \text{Fe}_2\text{O}_3$  (20 mTorr) and pure  $\text{BiFeO}_3$  (35 mTorr) thin films

### 3-5-2: Polarization electric field hysteresis loops (P-E)

Figure 3-5 shows the polarization electric field (P-E) hysteresis loops of the pure BFO and the BFO-Fe<sub>2</sub>O<sub>3</sub> nanocomposite films measured at 5 kHz at room temperature. The remnant polarization ( $P_r$ ) of the pure BFO thin film is  $7.2 \mu\text{C}/\text{cm}^2$  and the coercive field ( $E_c$ ) of pure BFO thin film is 470kV/cm when the maximum applied field is 500 kV/cm. The P-E loop of the pure BFO did not reach a saturated polarization because we could not apply an electric field higher than 500 kV/cm due to the high leakage current. There have been reports which suggest that the  $E_c$  of BFO may be intrinsically very high.<sup>51, 52, 53</sup> In contrast, the P-E loop of the BFO-Fe<sub>2</sub>O<sub>3</sub> nanocomposite thin film shows a more pronounced saturated polarization loop. The remanant polarization of the nanocomposite BFO thin film is  $49 \mu\text{C}/\text{cm}^2$ , and the coercive force 480 kV/cm with the maximum applied field of 925 kV/cm.

### 3-5-3: Remanent polarization ( $P_r$ ) as function of applied field.

The remanent polarization,  $P_r$ , as a function of applied electric field in the pure BFO and the BFO-Fe<sub>2</sub>O<sub>3</sub> nanocomposite thin films at 1 kHz at room temperature is shown in Fig. 3-6. The  $P_r$  of the pure BFO film begins increasing above an applied field of 250 kV/cm and continues to increase up to  $7.2 \mu\text{C}/\text{cm}^2$  at an applied field of 500 kV/cm. In this film, the low resistivity in the film makes it difficult to achieve a saturated polarization at room temperature. However, the BFO-Fe<sub>2</sub>O<sub>3</sub> nanocomposite thin film showed a much higher  $P_r$  ( $70 \mu\text{C}/\text{cm}^2$ ) at an applied field of 1000 kV/cm. The high resistivity in these films permits the application of an applied field twice as large

as that possible for pure BFO films. Also, the BFO - Fe<sub>2</sub>O<sub>3</sub> nanocomposite films may have larger E<sub>c</sub> than the pure BFO thin film because P<sub>r</sub> of nanocomposite films is lower than that of pure BFO at maximum applied field of 500 kV/cm. It is possible that Fe<sub>2</sub>O<sub>3</sub> may cause pinning of the ferroelectric domains in the films, thus making it difficult to switch domains. This indicates that the low leakage current of BFO - Fe<sub>2</sub>O<sub>3</sub> nanocomposite thin films showed a pronounced saturated polarization loop without stress. This suggests that the larger value of the remnant polarization is related to decreased leakage current rather than stress in the film.<sup>54, 55, 56</sup>

The origin of the lower leakage current in the nanocomposite films is not understood at this time. Atomic force microscopy of the nanocomposite films and the pure BFO films showed that the nanocomposite films have smoother surfaces with the average root mean square roughness of 2 nm (for 3×3 μm<sup>2</sup>), whereas pure BFO films have the average root mean square roughness of 10 nm. In dielectric/ferroelectric thin films, smoother films tend to display higher breakdown voltages with lower leakage currents. In general, rough surfaces tend to have higher densities of possible pinhole/leakage paths. It is not clear, however, how the nanocomposite films have smoother films. Perhaps the Fe<sub>2</sub>O<sub>3</sub> regions are playing the role of “plugging” up the grain boundaries between BFO grains, thus minimizing the leakage current. Further microstructural investigation is under- way to elucidate this mechanism.

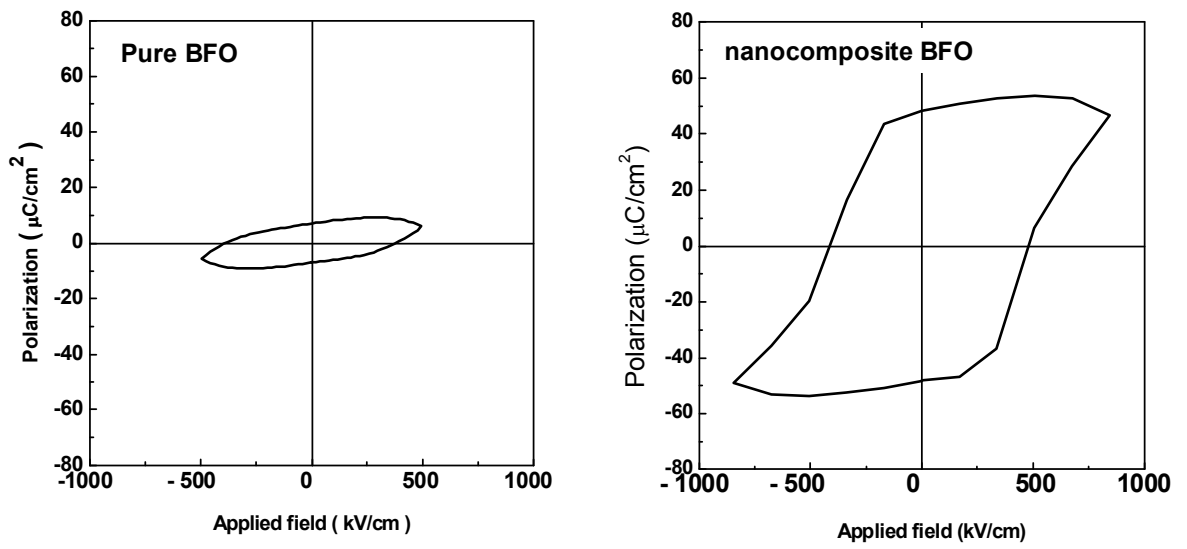


Figure 3-5. Polarization electric field (P-E) hysteresis loops of pure BFO and BFO -  $\text{Fe}_2\text{O}_3$  composite films measured at 5 kHz and at room temperature.

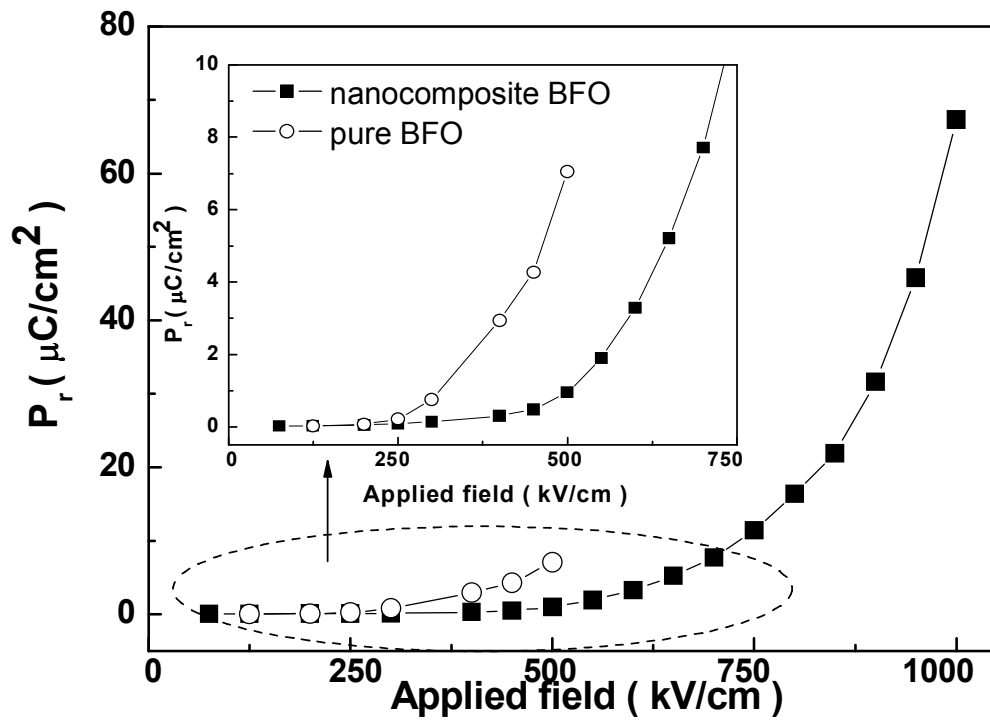


Figure 3-6. Remanent polarization ( $P_r$ ) as function of applied electric field in pure BFO and nanocomposite BFO- $\text{Fe}_2\text{O}_3$  thin films measured at a frequency of 1 kHz and at room temperature.

### **3-6: Conclusion**

In summary, we investigated the ferroelectric properties of the multiphase Bi-Fe-O thin film system. We found that the make up of the dominant phase in the films varies as a function of the deposition pressures and can be controlled by tuning the pressure. We observed a large remnant polarization ( $60 \mu\text{ C/cm}^2$ ) at an applied field of 1000 kV/cm in the BFO -  $\text{Fe}_2\text{O}_3$  nanocomposite thin films at room temperature. The nanocomposite films had a relatively low leakage current and were fully relaxed. Our result suggests that the enhancement of polarization is not stress related. The small amount of  $\text{Fe}_2\text{O}_3$  phase helps for improving electric properties, but the  $\text{Fe}_2\text{O}_3$  phase can not be detected using XRD since the  $\text{Fe}_2\text{O}_3$  grains are too small (100 nm ~ 200 nm). The BFO with  $\text{Fe}_2\text{O}_3$  films have smoother surfaces than the pure BFO. In general, rough surface tends to lead to a higher density of leakage paths. The smooth surface may be minimizing the leakage current.

## **CHAPTER 4. COMBINATORIAL DISCOVERY OF A MORPHOTROPIC PHASE BOUNDARY IN $\text{Bi}_{1-x}(\text{RE})_x\text{FeO}_3$ (RE : RARE EARTH) THIN FILM COMPOSITION SPREADS**

After finding the optimum deposition condition for the BFO thin films showing good ferroelectric properties (which include small amount of  $\text{Fe}_2\text{O}_3$ ), we started to explore rare earth doped BFO systems using binary composition spread thin films. We find that under the small amount of  $\text{Fe}_2\text{O}_3$  inclusion disappears as Bi is substituted with a rare earth dopant. This may be attributed to the fact that since Bi substitution reduces the amount of Bi, there is less need for Bi-deficiency induced  $\text{Fe}_2\text{O}_3$  formation. A number of interesting compounds were identified from our initial screening. In this study, we mainly focus on results from the  $\text{Bi}_{1-x}\text{Sm}_x\text{FeO}_3$  (BSFO) composition spread. We obtained several interesting results from this system. We found a new MPB in the system. At the MPB, we observed enhancement of ferroelectric properties. The MPB is a ferroelectric to antiferroelectric phase boundary.

## 4-1 Introduction

$\text{BiFeO}_3$  (BFO) is a multiferroic with rich and intricate physical properties.<sup>57</sup> Given the need for environmentally friendly lead-free piezoelectrics<sup>58</sup>, doped-BFO is being investigated for improved properties<sup>59, 60, 61</sup>, so that they may emulate the performance of Pb-based piezoelectrics<sup>62, 63</sup> at morphotropic phase boundaries (MPBs). However neither an increase in electromechanical constants as a function of dopant concentration or domain structures indicative of a MPB has been reported to date in BFO-based lead-free systems. There are some guidelines which predict the presence of MPBs<sup>64, 65, 66</sup> and one can explore novel compositions by systematically searching for similar structural transitions. We have applied the combinatorial strategy in the form of composition spreads.

## 4-2: Experimental procedure

Binary composition spread epitaxial thin film libraries (200 nm thick) were fabricated on  $\text{SrTiO}_3$  (001) substrates 6 mm long by the combinatorial pulsed laser deposition system (Pascal, Inc.), where a pseudo-binary compositional phase diagram of  $\text{Bi}_{1-x}\text{Sm}_x\text{FeO}_3$  was continuously mapped on each chip. Composition variation across the spreads were confirmed by an electron probe (JEOL JXA-8900), and the uncertainty in the composition at each point on the spread is +/- 1.5%. For the initial characterization of the films, we used piezo-resopnse force microscope to measure piezoelectric properties, and we used point by point X-ray microdiffraction to study the crystal structure of the films. Electrical properties (polarization, dielectric constant, and piezoelectric coefficient) were measured using a two capacitance method as shown

Figure 2-4. The size of electrode pad is 50  $\mu\text{m}$  by 50  $\mu\text{m}$  square. The pads covered the composition spread samples with a 100  $\mu\text{m}$  space from each other.

### **4-3: Microstructure of $\text{Bi}_{1-x}\text{Sm}_x\text{FeO}_3$ thin films**

#### **4-3-1: XRD of BSFO composition spread thin film.**

X-ray diffraction (XRD) mapping of the (002) peak region in a BSFO composition spread on [001]  $\text{SrTiO}_3$  (STO) are shown in Figure 4-1. Initial piezoforce microscopy (PFM) scans of a BSFO composition spread library indicated significant enhancement of piezoresponse near  $\text{Bi}_{0.8-0.85}\text{Sm}_{0.2-0.15}\text{FeO}_3$ , where the structure undergoes substantial change in the out-of-plane lattice constant. A detailed analysis of a series of two-dimensional XRD images of this composition region revealed appearance of extra diffraction spots for  $x \geq 0.13$  (shown in Figure 4-2), indicating a cell doubling structural transition to a lower symmetry phase. The structural transition is from a rhombohedral to an orthorhombic structure. It turns out that the structure right at this composition is triclinic, as identified using TEM (discussed in the next section and shown in Figure 4-3). The triclinic structure at this composition can be viewed as a cell doubling distorted rhombohedral structure or a distorted orthorhombic structure. To check to see if the structural transition is a morphotropic phase boundary (MPB), we measured a high temperature XRD of the same spread. We observed that the structural transition starts at approximately the same composition of  $x \approx 0.14$ , with no additional structural transitions up to the highest measured temperature of 400  $^\circ\text{C}$ . Thus, the transition takes place at the same composition regardless of temperature, and so we identify this to be a MPB.

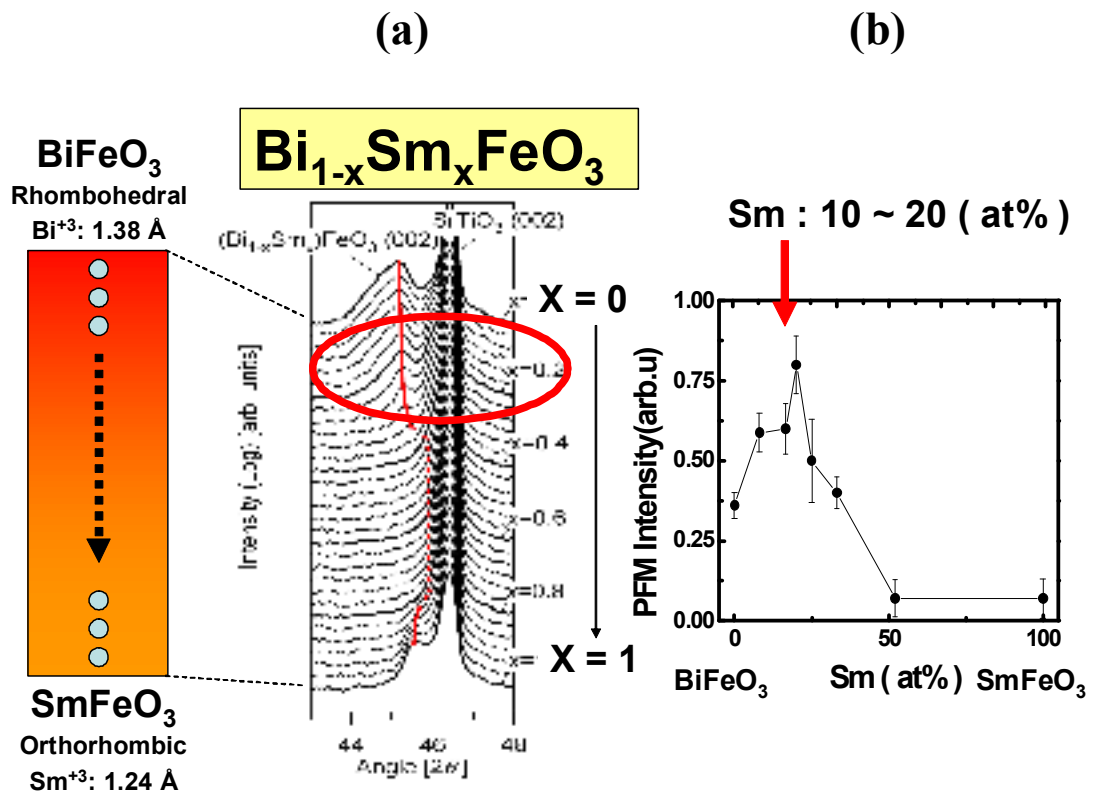


Figure 4-1.

X-ray diffraction and PFM mapping of  $\text{Bi}_{1-x}\text{Sm}_x\text{FeO}_3$  composition spread (a)  $\theta$ -  $2\theta$  scan from  $43^\circ$  to  $48^\circ$  across a composition spread (6 mm long) on [001]  $\text{SrTiO}_3$  shows continuous change in the film lattice constant (region circled in red). The red line traces the (002) peak of  $\text{Bi}_{1-x}\text{Sm}_x\text{FeO}_3$  except for the dotted region where the peak is obscured by the substrate peak. Initial piezoforce microscopy (PFM) mapping of piezo response from the BSFO composition spread (b).

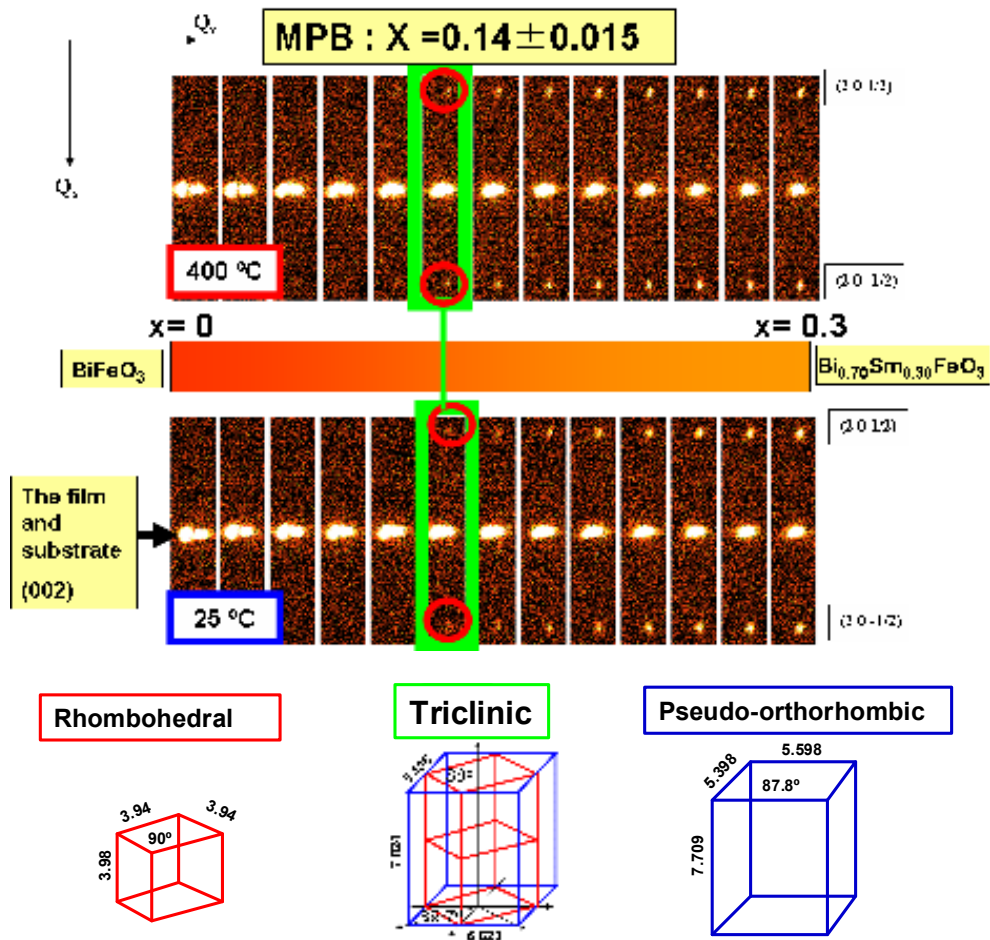


Figure 4-2.

Two-dimensional diffraction images ( $Q_z$ - $Q_x$ ) taken from  $x = 0$  to  $x = 0.3$  in  $\text{Bi}_{1-x}\text{Sm}_x\text{FeO}_3$  composition spread. The indexes are assigned using the perovskite (rhombohedral) structure. Beyond  $x \approx 0.13$ , the  $\text{Bi}_{1-x}\text{Sm}_x\text{FeO}_3$  (002) spot is a mixture of (002), (020), and (200) spots due to twinning. The  $(2\ 0\ 1/2)$  and  $(2\ 0\ -1/2)$  spots starting at  $x \approx 0.14$  indicate cell-doubling.  $\text{Bi}_{1-x}\text{Sm}_x\text{FeO}_3$  goes from rhombohedral  $\text{BiFeO}_3$  (unit-cell in red) to orthorhombic  $\text{SmFeO}_3$  (unit-cell in blue). Beyond  $x \approx 0.27$ , the compound is paraelectric.

#### 4-3-2: TEM of BSFO at MPB composition

High resolution planar transmission electron microscopy (A JEOL 2100 F operating at 200 kV) of an individual composition sample at  $x \approx 0.14$  (Figure.4-3) reveals presence of unusual nano-scale triclinic domains 20 – 50 nm in size displaying different relative epitaxial orientations. The lattice parameters of this composition were determined to be  $a = 5.62 \text{ \AA}$ ,  $b = 7.83 \text{ \AA}$ ,  $c = 5.50 \text{ \AA}$ ,  $\alpha = \gamma = 89.8^\circ$ , and  $\beta = 89.7^\circ$ . The occurrence of nanosized twins and concomitant stress accommodation have previously been identified as fingerprints of an adaptive ferroelectric phase at the MPB, which could result in a high piezoelectric coefficient and narrow hysteresis loops.<sup>20</sup> These nanodomains are observed only at this composition, and for  $x$  outside of  $0.14 \pm 0.015$ , the domains were found to be much larger in size ( $\sim 100 \text{ nm}$ ).

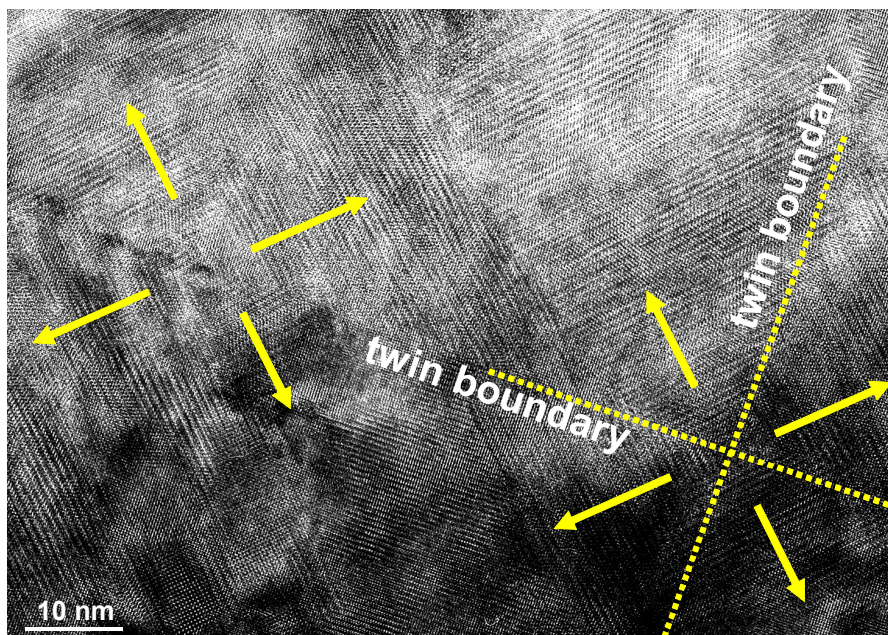


Figure 4-3.

High resolution plan-view transmission electron microscopy image of the composition at the morphotropic phase boundary (MPB,  $x = 0.14$ ). The triclinic nanodomains 20-50 nm in size are observed with twin boundaries (yellow dotted lines).

## 4-5: Ferroelectric and antiferroelectric in $\text{Bi}_{1-x}\text{Sm}_x\text{FeO}_3$ thin films.

### 4-5-1: P-E loops of BSFO thin films

Square-shaped ferroelectric hysteresis loops with good saturation and robust switchable polarization are obtained for compositions from  $x = 0$  up to  $x \approx 0.14$ . Figure 4-4 plots hysteresis loops at room temperature for three compositions (BFO,  $\text{Bi}_{0.86}\text{Sm}_{0.14}\text{FeO}_3$  and  $\text{Bi}_{0.84}\text{Sm}_{0.16}\text{FeO}_3$ ) selected for displaying the most prominent features. While increasing the Sm concentration induces a large drop in the coercive field from 420 kV/cm to 160 kV/cm. The value of polarization remains the same ( $\approx 70 \mu\text{C}/\text{cm}^2$ ). Thus, we are able to demonstrate a high switchable polarization and a low coercive field at the MPB. On the other side of the MPB ( $x \geq 0.15$ ), we observe double hysteresis loops, indicative of an antiferroelectric (AFE) behavior<sup>10, 67</sup>. It is important to note that the AFE composition at  $x \approx 0.16$  still maintains a relatively high polarization once electric-field induced switch to FE takes place. These hysteresis curves do not change their shapes with time (over 6 months) or the number of measurement cycles (10s of cycles for each measurement), indicating that the double hysteresis loops are not from domain-wall pinning.

The present results show that  $\text{Sm}^{+3}$  substituted BFO has unique properties compared to more popular lanthanum (La)<sup>68</sup> or neodymium (Nd)<sup>61, 62</sup> doped BFO. It was reported that 5% substitution of La (or Nd) in BFO thin films resulted in reduction of the crystal anisotropy by more than 10% accompanied by a drastic reduction in the switchable polarization (from  $79 \mu\text{C}/\text{cm}^2$  to  $40 \mu\text{C}/\text{cm}^2$ ).<sup>62</sup> However, no distinct increase in the electromechanical properties or the occurrence a complex domain

structure was reported. Suchomel and Davies have shown that any advantage gained by introducing a structural phase transition via doping with a non-lone pair cation is offset by the dramatic reduction in polarization due to the nonpolarizable dopant, as is the case for  $\text{La}^{+3}$ .<sup>69</sup> Further,  $\text{Sm}^{+3}$  (1.24 Å) has a much smaller ionic size than  $\text{La}^{+3}$  (1.36 Å). Thus, the Goldschmidt tolerance factor<sup>70</sup> for the  $\text{Sm}^{+3}$  doped BFO is less than 1, and lower symmetry structures such as triclinic are more likely at the MPB. The presence of a low symmetry phase at the MPB is expected to enhance the piezoelectric properties as the polarization vector is no longer constrained to lie along a symmetry axis but instead can rotate within a suitable plane.<sup>69, 71, 72, 73</sup>

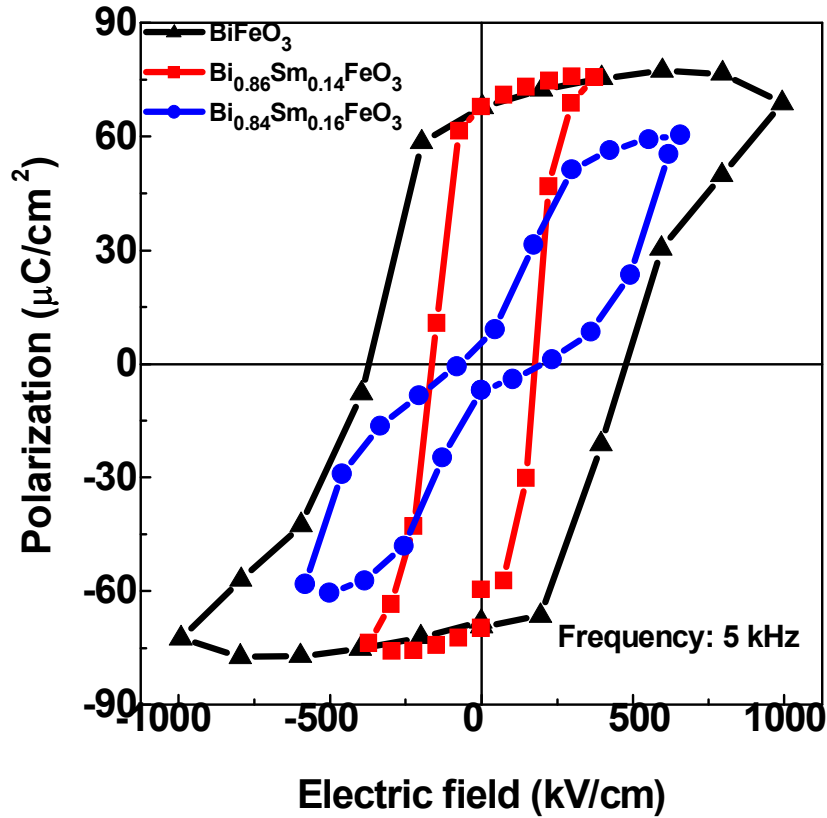


Figure 4-4.

Continuous change in the ferroelectric hysteresis loops (5 kHz) is observed as a function of changing composition. Three representative compositions were selected for display for clarity. The relatively high polarization of  $\approx 70 \mu\text{C}/\text{cm}^2$  is maintained as we go from BiFeO<sub>3</sub> to Bi<sub>0.86</sub>Sm<sub>0.14</sub>FeO<sub>3</sub>. Beyond MPB and until  $x \approx 0.27$ , the material displays antiferroelectric (AFE) characteristics (as seen for  $x = 0.16$ ).

#### **4-5-2: Dielectric constant as a function Sm content.**

At the MPB, the crystal structure is changing. Therefore we expect a peak in dielectric constant at the structural phase boundary. Figure 4-5 shows the dielectric constant and loss tangent measured at 10 kHz as a function of Sm concentration. The dielectric constant continuously increases up to 14% Sm. At this composition, the dielectric constant is 420. This is the same composition as the structural transition composition. The loss tangent at this composition is relatively low ( $\sim 0.01$ )

#### **4-5-3: Piezoelectric coefficient $d_{33}$ as a function of Sm content.**

At the MPB, we observed peaking of dielectric constant. We also expect to see enhancement of the piezoelectric constant ( $d_{33}$ ) and reduction of coercive field ( $E_c$ ) at the structural phase boundary. The  $d_{33}$  and  $E_c$  were determined from the piezoelectric hysteresis loops measured using a piezoforce microscope (PFM). Figure 4-6 plots the high-field  $d_{33}$  as a function of Sm doping. Around  $x = 0.13 \sim 0.15$ , the effective  $d_{33}$  displays a rapid increase peaking at  $x = 0.14$  with 110 pm/V. Also, the composition near the MPB possesses a substantially lower coercive field ( $E_c = 70$  kv/cm) compared to that of pure BFO.

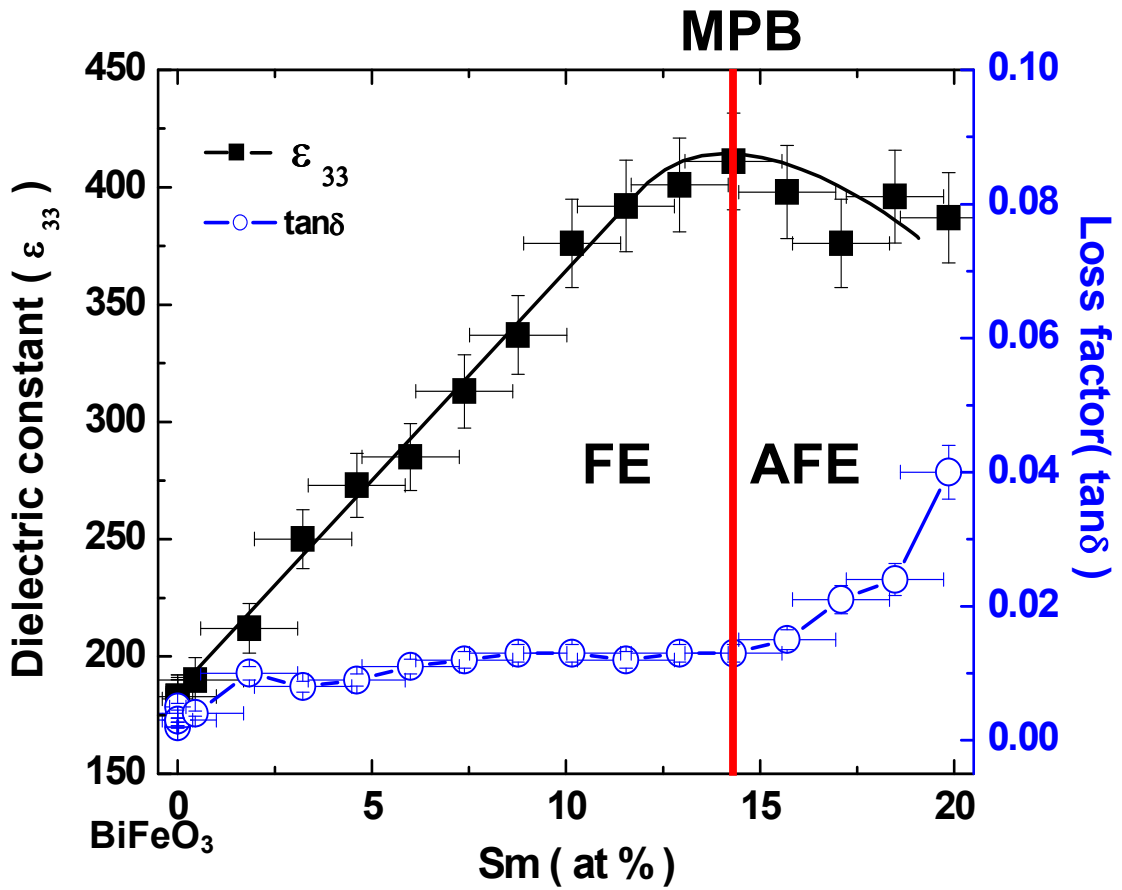


Figure 4-5.

Dielectric constant ( $\epsilon_{33}$ ) and  $\tan \delta$  measured at 10 kHz (zero-bias).  $\epsilon_{33}$  shows a broad peaking behavior with a maximum at  $x = 0.14$ , while the loss tangent remains relatively low. The curve is a guide to the eye.

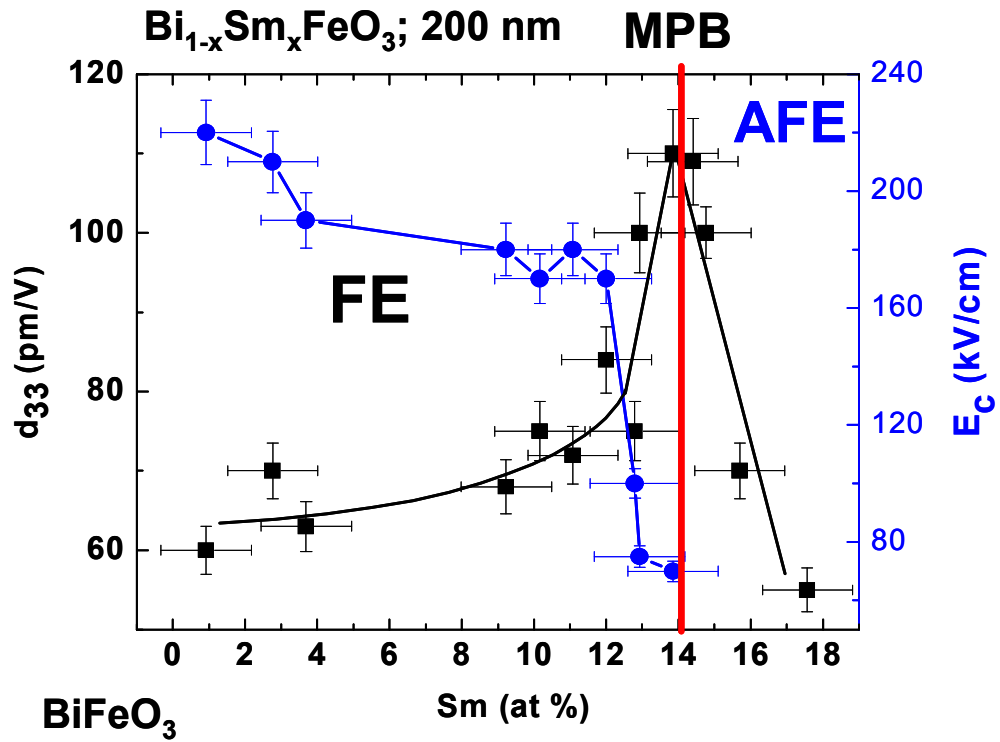


Figure 4-6.

High-field piezoelectric coefficient ( $d_{33}$ ) and coercive field ( $E_c$ ) determined from the piezoelectric hysteresis loops measured as a function of composition. The average value obtained for the positive and negative field is plotted. The  $d_{33}$  constant shows a sharp peak at  $x = 0.14$ .

#### **4-5-4: $d_{33}$ loops for $\text{BiFeO}_3$ and $\text{Bi}_{0.86}\text{Sm}_{0.14}\text{FeO}_3$**

Figure 4-7 shows the piezoelectric hysteresis loops of BSFO with  $x = 0$  and  $0.14$  measured via quantitative piezo force microscopy, which was performed on Pt/BSFO/SrRuO<sub>3</sub> (SRO)/STO structures using Pt-Ir coated contact mode tips<sup>74</sup>. The measured  $d_{33}$  values are effective values due to the constraint imposed by the underlying substrate. The composition right near the MPB possesses a substantially higher remanent out-of-plane  $d_{33}$  ( $\sim 95$  pm/V) together with much reduced coercive field compared to that for  $x = 0$ . The remanent  $d_{33}$  for a (001) oriented epitaxial PbZr<sub>0.52</sub>Ti<sub>0.48</sub>O<sub>3</sub> thin film with the same nominal thickness (200 nm) is 100 pm/V.<sup>19</sup>

#### **4-5-5: Rayleigh analysis of the measured out-of-plane piezoresponse for the MPB composition ( $\text{Bi}_{0.86}\text{Sm}_{0.14}\text{FeO}_3$ )**

To determine if the observed piezoelectric behavior of the BSFO thin film is an intrinsic or extrinsic phenomenon, we performed the Rayleigh analysis<sup>75</sup> on the measured out-of-plane piezoresponse for the MPB composition ( $\text{Bi}_{0.86}\text{Sm}_{0.14}\text{FeO}_3$ ) sample (shown in Figure 4-8). It shows that the magnitude of the piezoelectric coefficient scales linearly with the amplitude of the excitation sub-coercive ac electric field, while the second and third harmonic components are less than 1% of the total response even for high ac field. This behavior is quite different from the dynamic poling behavior observed in Pb-based piezoelectric thin films<sup>20</sup>. The lack of non-linear response in the first harmonic clearly suggests absence of any non-180° domain wall

motion (pinned due to the substrate-induced constraint), and the near-zero second harmonic response indicates negligible electrostriction in this material.

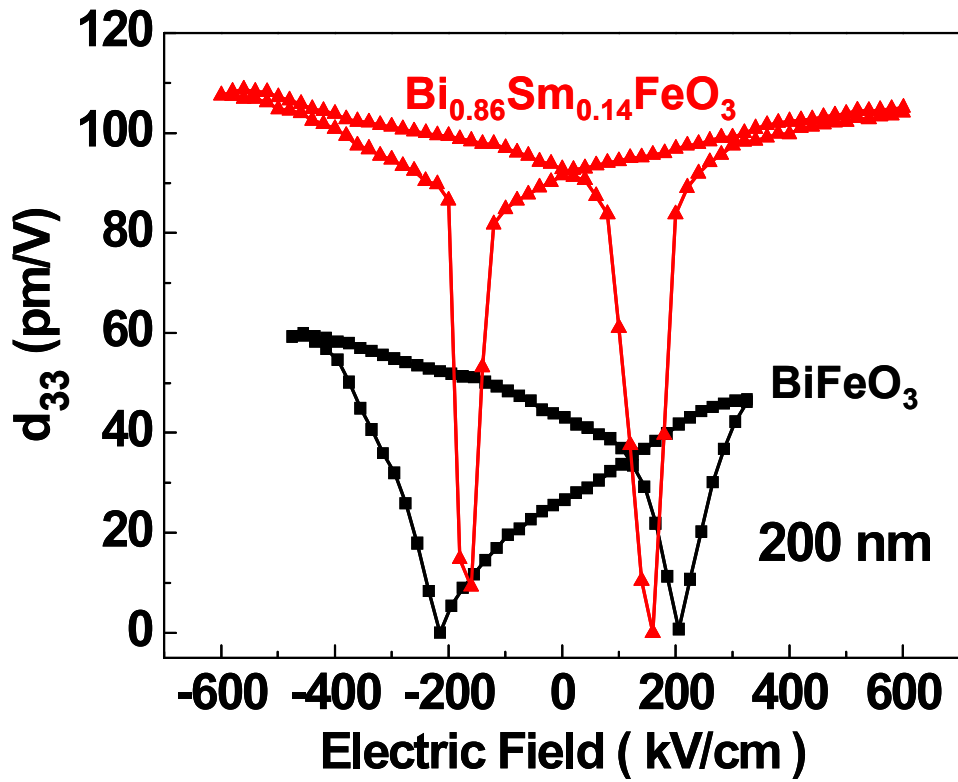


Figure 4-7.

Piezoelectric properties of  $\text{Bi}_{1-x}\text{Sm}_x\text{FeO}_3$   $d_{33}$  loops for  $\text{BiFeO}_3$  and  $\text{Bi}_{0.86}\text{Sm}_{0.14}\text{FeO}_3$ .

The high value of remanent  $d_{33}$  for  $\text{Bi}_{0.86}\text{Sm}_{0.14}\text{FeO}_3$  is comparable to that of PZT thin films of the same thickness at MPB.

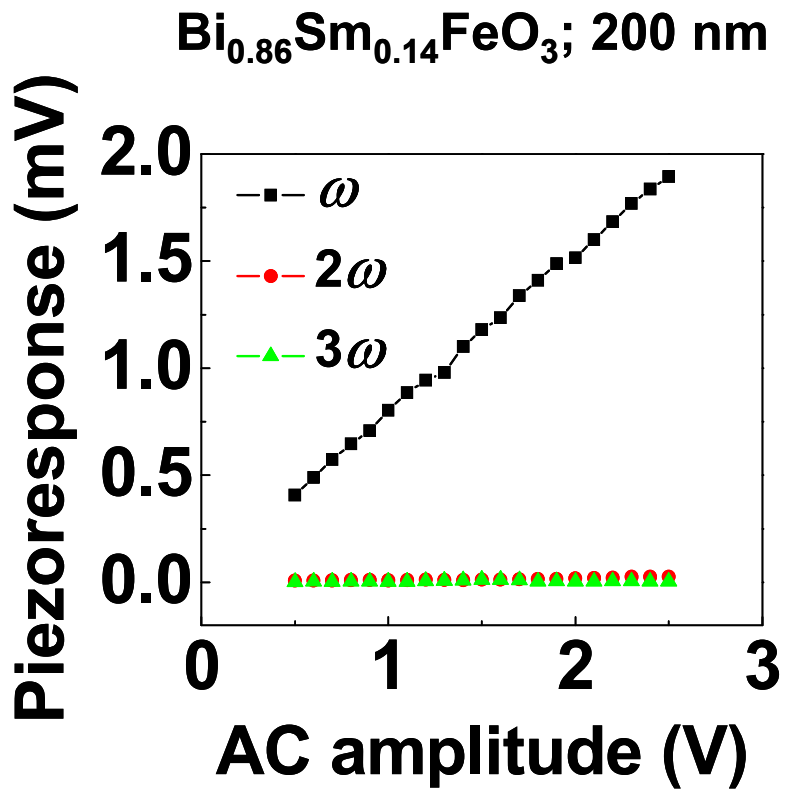


Figure 4-8. Rayleigh analysis measurements for the MPB composition sample.

First harmonic ( $1\omega$ ) is modulated by the reflection of a laser beam signal. Also, the second harmonic signal if it exists related to the electrostrictive and dielectric permittivity.

#### **4-5-6: Capacitance as a function of DC bias-voltage (C-V) curve of antiferroelectric part of thin film.**

We see a double hysteresis behavior in the P-E loop as shown in Figure 4-4. This is a typical characteristic of an AFE material. We have measured the capacitance as a function of external DC bias voltage at the antiferroelectric composition. The capacitance was measured using a modulation voltage of 100 mV at 10 kHz. Figure 4-9 shows the  $\epsilon_{33}$  determined from the capacitance versus electric field curve obtained for the  $\text{Bi}_{0.84}\text{Sm}_{0.16}\text{FeO}_3$  composition. There is a double peaking behavior, which is a characteristic of AFE materials.

#### **4-5-7: $d_{33}$ loop for antiferroelectric part of thin film.**

We can relate the dependence of  $d_{33}$  on the applied electric field due to intrinsic domain reversal (i.e. no contributions such as ferroelastic motion or field-induced phase transitions) along the [001] direction of the film, using <sup>76</sup>:

$$d_{33}(E) = 2\bar{Q}P(E)\epsilon_{33}(E), \quad (1)$$

where  $P (= P_3)$  is the polarization and  $\epsilon_{33}$  is the relative dielectric constant.  $\bar{Q}$  is an effective electrostrictive coefficient that accounts for the clamping effect of the substrate. This phenomenological relation states that the field dependence of the  $d_{33}$  coefficient is principally governed by the field dependence of the polarization as well as the dielectric susceptibility. The main features of the AFE  $d_{33}$  loop are consistent with the  $P$ - $E$  loop (Fig. 4-4) and the  $\epsilon_{33}$ - $E$  curve (Fig. 4-9). As one can see in Figure 4-10, the black arrow marks the region where the electric-field induced transition from the

antiferroelectric to ferroelectric state is taking place. The eventual maximum in the  $d_{33}$  loop is a consequence of the increase in the switching polarization in the ferroelectric state with a sharp positive change of the slope of the  $P$ - $E$  loop and increase in the dielectric susceptibility at that point. As the applied electric field increases further, an inflection point is reached beyond which the net increment in switchable polarization for given increase in applied field begins to decrease. As a consequence, the dielectric susceptibility begins to decrease, and hence also brings down the  $d_{33}$  value (the red arrow). At higher electric field, the polarization is fully switched and now similar to a “fully saturated state” in a standard ferroelectric. Here, the drop in the dielectric susceptibility with increasing electric field dominates the shape of the  $d_{33}$  loop, which shows a downward slope (the green arrow).

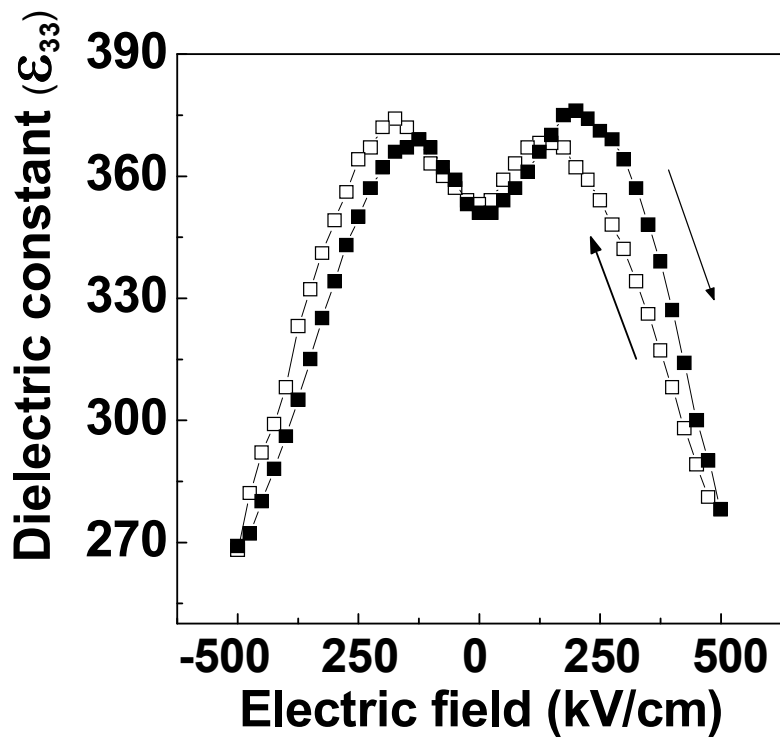


Figure 4-9.

Capacitance vs. electric field for the antiferroelectric (AFE) composition at  $\text{Bi}_{0.84}\text{Sm}_{0.16}\text{FeO}_3$ .

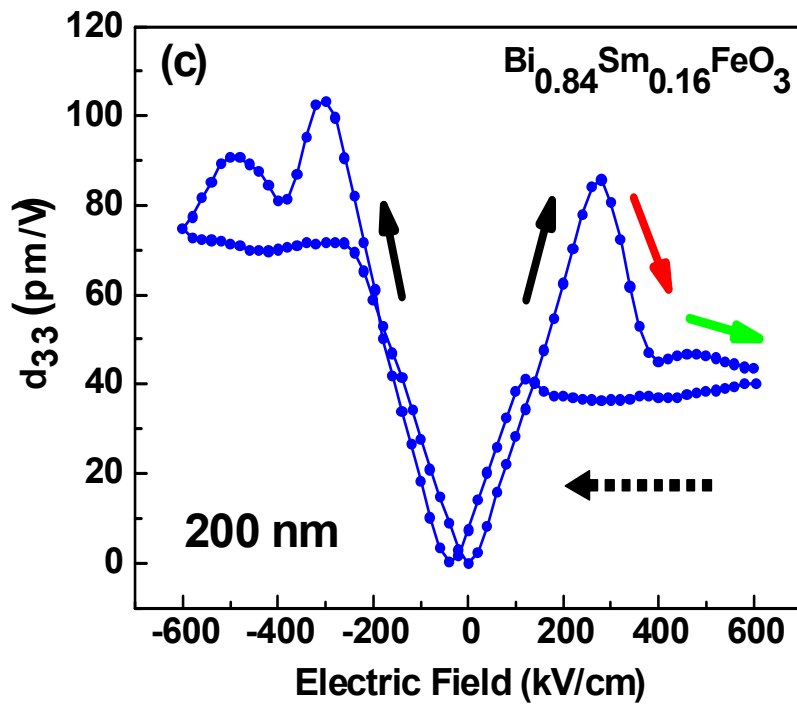


Figure 4-10.

Antiferroelectric  $d_{33}$  loop is observed for  $\text{Bi}_{0.84}\text{Sm}_{0.16}\text{FeO}_3$ . The black arrow marks the region where the electric-field induced transition from the antiferroelectric to ferroelectric state, the dielectric susceptibility begins to decrease, and hence also brings down the  $d_{33}$  value (the red arrow), and the drop in the dielectric susceptibility with increasing electric field dominates the shape of the  $d_{33}$  loop, which shows a downward slope (the green arrow).

#### 4-6. Other possible MPBs in other rare earth doped (La, Gd, Dy, and Lu) BiFeO<sub>3</sub>

Ravindran *et al*<sup>77</sup> have recently shown through density functional calculations that BFO undergoes a rhombohedral (R3c) to orthorhombic (Pnma) structural transition under pressure in Figure 4-11. In the Sm doped case, because of the small ionic radius, chemical pressure due to the continuous Sm<sup>+3</sup> substitute can perhaps be viewed as resulting in the similar lattice instabilities.

BSFO exhibits property enhancement at MPB. This is due to the chemical pressure due to the differences in the ionic radius since the Sm<sup>+3</sup>(1.24 Å) ion is smaller than the Bi<sup>+3</sup>(1.38Å) ion. So, by using other rare earth dopants with even smaller radii than Sm<sup>+3</sup>, we should be able to move the composition of MPB toward lower dopant concentration. The smaller amount of the dopants can perhaps maintain a higher polarization (due to the higher concentration of Bi) with low coercive field.<sup>23</sup> This simple idea and speculation is represented in Figure 4-12.

The BSFO composition spread film shows the extra spots starting at 14% Sm concentration which indicates cell doubling of a distorted rhombohedral or transiting to a distorted orthorhombic. We would expect to see the same transition occurring at lower dopants concentration if substitution with other RE elements with smaller ionic radii were carried out.

Figure 4-13 shows the out of plane lattice constant mapped in other RE doped BFO composition spread thin film using scanning X-ray microdiffraction. Different color data markers denote different dopant elements. Ionic radii decrease from 1.36 Å for La<sup>+3</sup> to 1.14 Å for Lu<sup>+3</sup>. Within a system, increasing the dopant concentration

decreases the lattice constant. We use the appearance of the extra spots in the diffraction images as the indication of the occurrence of the cell-doubling structural transition. Indeed, we find that the concentration at which the extra spots occur moves to the lower concentration by doping smaller ions radii elements. The start of the structural transition depends on the ionic radius. Also, we observed very similar trends in other rare earth doped BFO systems in ferroelectric properties compared to BSFO. The Gd doped BFO shows a large decrease in  $E_c$  from 514 kV/cm to 155 kV/cm with high polarization value ( $\approx 90 \mu\text{C}/\text{cm}^2$ ). Also, the Dy doped BFO displays clear a double hysteresis loop indicating atiferroelectric behavior as shown in Figure 4-14. From these results, we expect that these other RE doped BFO systems also have MPBs but at lower dopant concentration than  $\text{Sm}^{+3}$  doped due to smaller ionic radii. More detailed work are being carried out to confirm this.

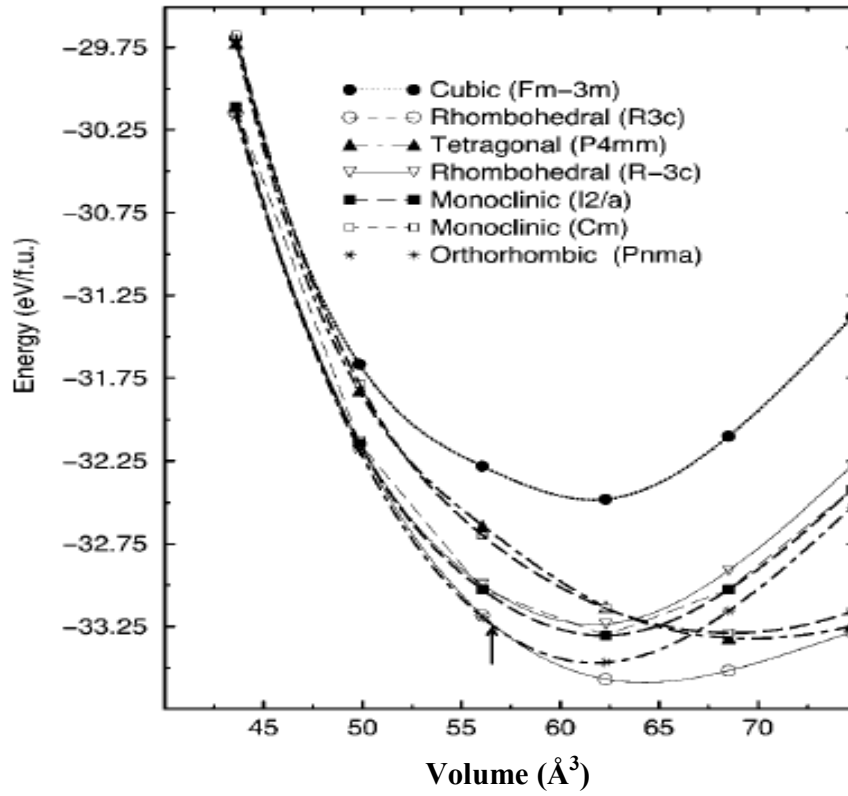


Figure 4-11.

Calculation of cell volume vs total energy for antiferromagnetic  $\text{BiFeO}_3$  in different possible structural arrangements [Ref. 78]

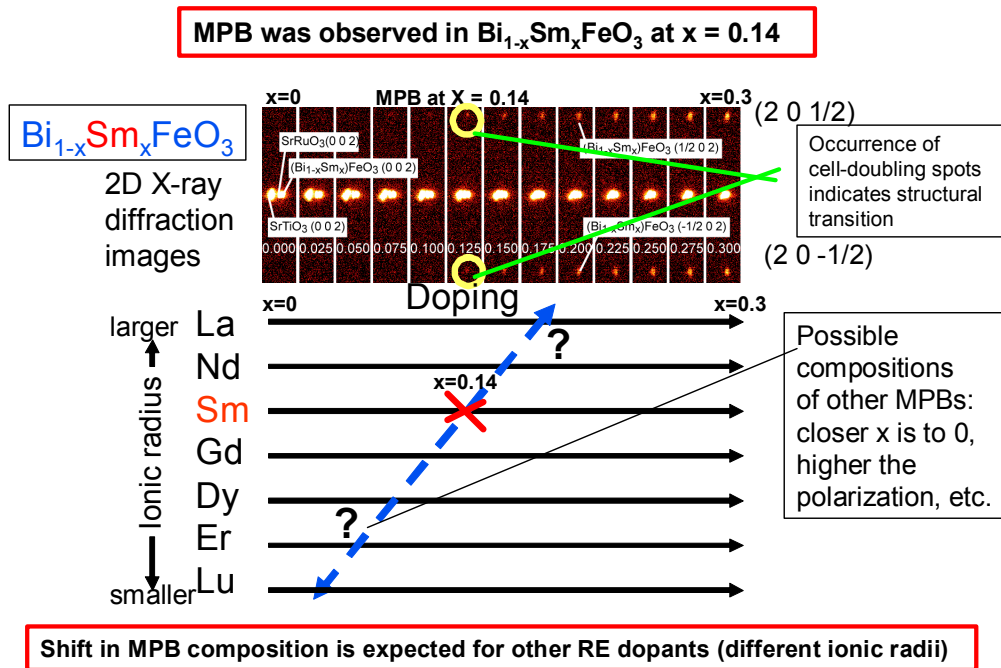


Figure 4-12.

Strategic scheme of search for other possible MPBs for other rare earth doped  $\text{BiFeO}_3$

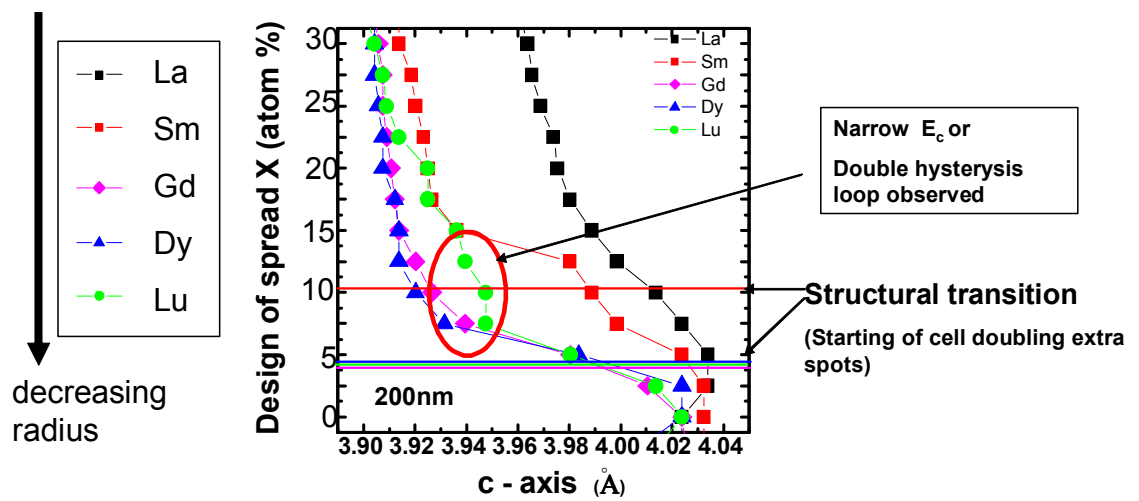


Figure 4-13.

Out-of-plane lattice constant mapped by scanning XRD for other rare earth doped

$\text{BiFeO}_3$  composition spreads  $\text{Bi}_{1-x}\text{RE}_x\text{FeO}_3$

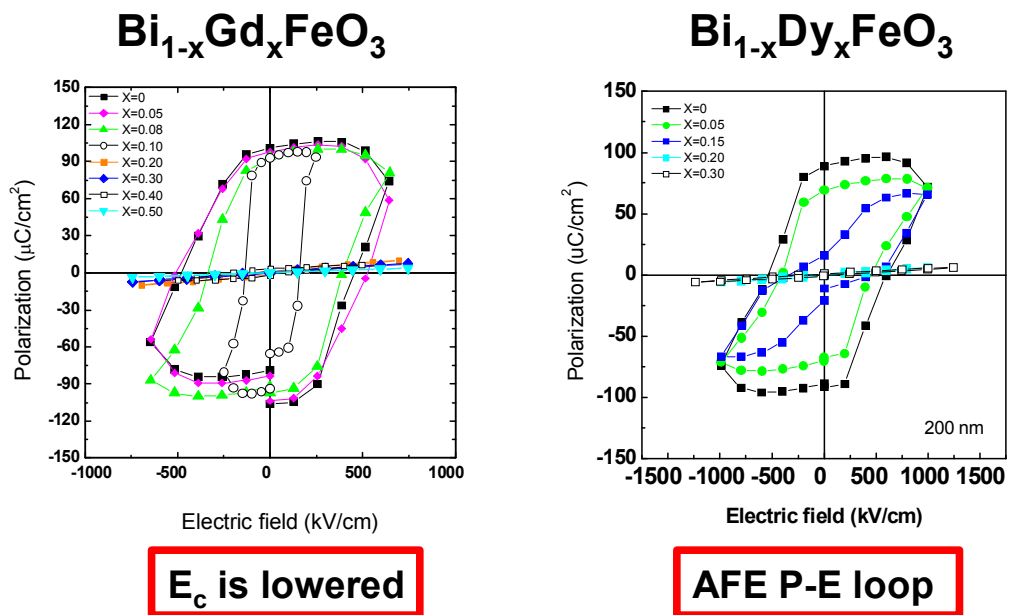


Figure 4-14.

P-E loops from other rare earth doped BiFeO<sub>3</sub> measured from other compositions from respective composition spreads. Similar properties seen in the BSFO system such as reduction of E<sub>c</sub> and occurrence of AFE hysteresis loops are observed here.

## 4-7: Conclusion

We have systematically investigated  $\text{Bi}_{1-x}(\text{RE})_x\text{FeO}_3$  using the thin film composition spreads technique. A number of interesting compounds were identified from our initial screening. We focused on results from the  $\text{Bi}_{1-x}\text{Sm}_x\text{FeO}_3$  (BSFO) composition spread. We obtained several interesting results from this system. We found a new MPB in the system. At the MPB, we observed enhancement of FE properties. The MPB is a FE to AFE phase boundary. The measured remnant and high field  $d_{33}$  are comparable to values previously reported for epitaxial thin films of Pb-based compounds such as  $\text{PbZr}_{0.42}\text{Ti}_{0.58}\text{O}_3$ . Domain engineered single crystals are known to exhibit enhanced electromechanical properties, but this is due to extrinsic mechanisms, which are generally absent in thin films<sup>20</sup>. In comparing nominally similar thin film samples of the same thickness, the BSFO thin film at the MPB discovered exhibits intrinsic piezoelectric properties which are among the best. The added advantage of the present system is a simpler crystal chemistry than some of the reported Pb-free compounds as well as ease of processing.<sup>64-66</sup> The simple perovskite-based BSFO at this MPB is a robust Pb-free piezoelectric. In addition, the unique composition and electric field tunable AFE/FE transition in BSFO may perhaps be used to engineer novel non-linear devices for energy storage and transducer applications<sup>78</sup>. We have also performed preliminary investigation on composition spreads with other rare earth dopants. These results indicate that the occurrence of the MPB and the structural transition is due to the chemical pressure effect and that there are similar MPBs with BFO doped with other RE dopants.

## CHAPTER 5. CONCLUSIONS AND FUTURE WORK

### 5-1. Conclusions

In the course of this study, we have discovered a lead-free MPB with a simple perovskite structure using the composition spread thin film strategy. We have found a rhombohedral to pseudo-orthorhombic structural transition in the  $\text{Bi}_{1-x}\text{Sm}_x\text{FeO}_3$  system which exhibits a ferroelectric to antiferroelectric transition at approximately  $\text{Bi}_{0.86}\text{Sm}_{0.14}\text{FeO}_3$  with dielectric constant and out-of-plane piezoelectric coefficient comparable to those of  $\text{Pb}(\text{Zr},\text{Ti})\text{O}_3$  thin films at the MPB.

The main findings of this thesis work can be summarized as follows.

- (i) We investigated the ferroelectric properties of multiphase  $\text{BiFeO}_3$  thin films grown under varying oxygen deposition pressures. The dominant phases produced in the film continuously change from a mixture of  $\text{BiFeO}_3$  with  $\text{Bi}_2\text{O}_3$  to a mixture of  $\text{BiFeO}_3$  with  $\text{Fe}_2\text{O}_3$  as the oxygen deposition pressure is varied. X-ray diffraction and transmission electron microscopy revealed that epitaxial  $\text{BiFeO}_3$  and  $\text{Fe}_2\text{O}_3$  were grown when the deposition pressure was  $\approx 20$  mTorr and the  $\text{BiFeO}_3$  grains were completely relaxed from epitaxial strain. The film made under this deposition condition exhibits a high switchable polarization ( $60 \mu\text{C}/\text{cm}^2$ ) and a low leakage current density ( $\approx 1 \times 10^{-4} \text{ A}/\text{cm}^2$  at 250 kV/cm) at room temperature.
- (ii) We made the composition spread thin film of  $\text{Bi}_{1-x}\text{Sm}_x\text{FeO}_3$  (BSFO) to systematically investigate crystal structure in detail using XRD and TEM. The

XRD revealed the occurrence of a structural phase transition at  $x = 0.14$ . The phase transition at this composition is from a rhombohedral to an orthorhombic structure. It turns out that the structure right at this composition is triclinic using TEM. Also, we measured high temperature XRD at 400 °C and observed that the phase transition takes place at the same composition as at room temperature. Thus, we identify this to be a morphotropic phase boundary (MPB).

- (iii) In the BSFO, square-shaped hysteresis loops are obtained for compositions up to 14% Sm content, indicating presence of a robust ferroelectric phase. Substitution Sm for Bi the Sm content induces a large drop in the coercive field ( $E_c$ ) from 420 kV/cm to 160 kV/cm. The value of  $E_c$  is the smallest compared with other reported BFO based materials. Thus, we are able to demonstrate a high switchable polarization and a low coercive field at the MPB.
- (iv) On the other side of the MPB ( $x > 0.14$ ), we observe a double-loops shaped P-E hysteresis characteristics, which is characteristic of an antiferroelectric (AFE) behavior. Compared to the ferroelectric phase, the value of the switchable polarization is still relatively high ( $\approx 75\mu\text{C}/\text{cm}$  at  $\approx x = 0.16$ ). We measured capacitance as a function of voltage and observed a double peaking behavior, which is a characteristic of AFE materials. We also measured  $d_{33}$

loops for the film. The unique shape we see here is also indicative of an AFE phase.

- (v) At the MPB, the intrinsic piezoelectric coefficient of  $d_{33}$  is approximately 110 pm/V at high field. The BSFO thin films increase in the  $d_{33}$  as well as a decrease in the coercive field as the MPB composition is approached. The intrinsic  $d_{33}$  for an epitaxial  $\text{PbZr}_{0.42}\text{Ti}_{0.58}\text{O}_3$  (PZT) thin film at the MPB with the same thickness is 160 pm/V. The  $d_{33}$  for BSFO at the MPB is comparable to PZT. Thus, BSFO is a strong candidate of a Pb-free piezoelectric material.
  
- (vi) We have found that the smaller ionic radii RE dopants other than Sm can induce structural transitions at lower dopant concentration. We obtained preliminary data which indicate that the start of structural transition composition depends on ionic radii of the dopants. Other rare earth (RE) doped  $\text{BiFeO}_3$  (BFO) exhibit similar FE/AFE characteristics such as large decrease in coercive field and the presence of double hysteresis loops which indicate the characteristic of atiferroelectric phase. From these results, the initial indication is that other RE doped BFO systems also have similar MPBs.

## **5-2. Possibility applications of MPB BSFO and future work**

In the modern society, everyone use a computer at least once a day for checking e-mail, reading news, watching videos, searching for information, and so on. Reduction of waiting time while using a computer was the most desirable improvement issue for PCs found in a recent web-based survey.<sup>79</sup> For example, when we turn on a computer, we have to wait a short time for the machine to start up. It is desirable to shorten this time. Non-volatile random access memories (NVRAM) can solve the boot-up time problem because the information stored in NVRAM is not lost when power is turned off. Since information is not lost during power-down, a computer using NVRAM could be powered off one day and then turned on the next day and be in exactly the same state, without taking any time for shut-down or boot-up.

There are four main types of NVRAM devices: flash, which is based on the floating gate transistor using an insulating material<sup>80</sup>, phase change random access memory (PRAM), which is based on changing the crystal structure of a material<sup>81</sup>, ferroelectric random access memory (FeRAM), which is based on ferroelectric material<sup>82</sup>, and magnetoresistive random access memory (MRAM),<sup>83</sup> which is based on a ferromagnetic and antiferromagnetic multilayer.

BSFO thin films have both a large value of switchable remnant polarization and antiferromagnetic properties at room temperature and are therefore potentially useful for both FeRAM and MRAM. Future work should be focused on the integration of BSFO thin films into such memory devices.

### 5-2-1. New multiferroic spintronic device

One well known application of antiferromagnetic (AFM) materials is exchange bias in spin valve devices.<sup>84</sup> Recently, we came up with a design for a multiferroic spintronic device as shown in Figure 5-3.<sup>85,86</sup> Here, we propose to use BSFO as the AFM pinning layer in the spin valve structure. If BSFO displays magneto-electric (ME) coupling<sup>87</sup>, the exchange coupling between the ferromagnetic and the AFM layer could be changed by applying an electric field. (At the time of this writing, the presence of robust ME coupling in BFO and related compounds has not been definitively established). Furthermore, since BSFO is a good ferroelectric, we can also use this layer as a ferroelectric memory element. Thus, we have the possibility to combine a tunable magnetic memory element with a ferroelectric polarization memory element in one and the same structure.

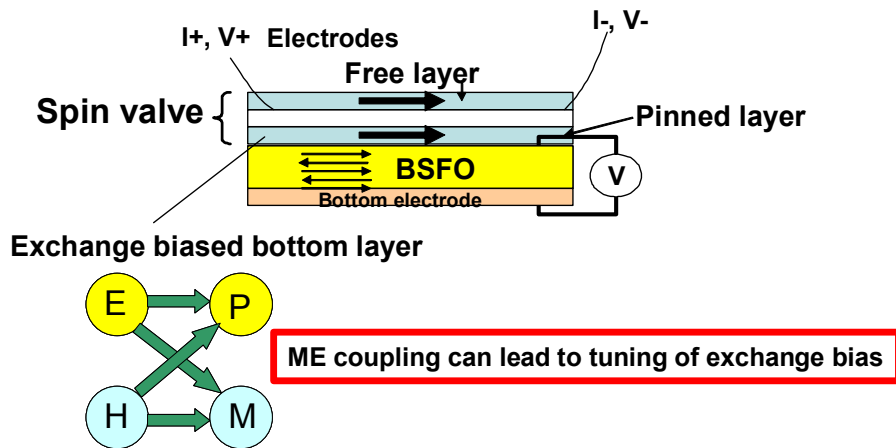


Figure 5-1 Schematic of a multiferroic spintronic device structure

### 5-2-2. Non-volatile ferroelectric random access memory device (FeRAM).

Strontium bismuth tantalum (SBT)<sup>88</sup> and lead zirconate titanate (PZT)<sup>86</sup> are now used as ferroelectric materials for FeRAMs. However, these materials have a relatively lower-charge storage capability which comes from a low polarization (10~ 40  $\mu\text{C}/\text{cm}^2$ ).<sup>89</sup> Therefore, the existing FeRAM has a scalability problem. The technological limit of these devices due to this problem is expected to occur at the 130 nm node because of the decreasing cell area. This limit is expected to be reached in 2009.<sup>86</sup> So, in order to continue increasing storage density in FeRAM, we require a higher polarization material. On August 2, 2006, Fujitsu reported a new generation FeRAM using manganese (Mn) doped  $\text{BiFeO}_3$ . Using this new material it is possible to increase data storage density by up to five times compared to the current materials.<sup>90</sup> These new devices can provide memory cell capacities of 256 Mbits using the 65 nm node technology. The drawback of Mn doped BFO is that it may have a large coercive field. BSFO has the smallest coercive field of all BFO based materials. Thus, using BSFO, it is expected that we can decrease power consumption.

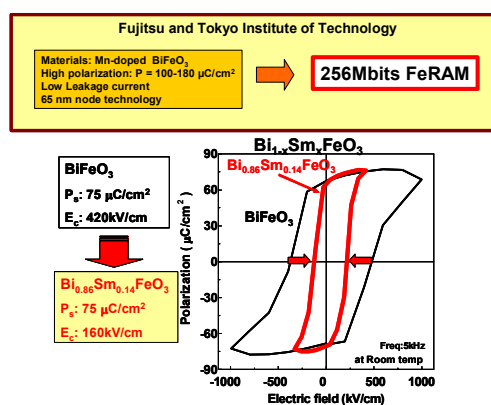


Figure 5-2. Approach to FeRAM devices

## BIBLIOGRAPHY

- 
- <sup>1</sup>European Union: Waste Electrical and Electronic Equipment (WEEE)  
<http://eurlex.europa.eu/LexUriServ/LexUriServ.do?uri=CELEX:32002L0096:EN:NOT>
- <sup>2</sup> Japan Electronics and information Technology Industries Association (JEITA),  
<http://www.jeita.or.jp/english/>
- <sup>3</sup>B. A. Strukov and A. P. Levanyuk, *Ferroelectric Phenomena in Crystal*, ISBN:3-540-63132-1, Springer-Verlag Berlin Heidelberg New York (1998).
- <sup>4</sup> C. Kittel, *Introduction to Solid State Physics*, ISBN: 0-471-11181-3, John Wiley & Sons( 1996).
- <sup>5</sup>B. Jaffe, *Proceeding of the IRE*, 1464 (1960).
- <sup>6</sup>G. Shirane, E. Sawaguchi, and Y. Takagi, *Phys. Rev*, vol 80,485 (1950).
- <sup>7</sup> K. Uchino, *Ferroelectric devices*, ISBN: 0-8247-8133-3, Marcel Dekker, Inc (2000).
- <sup>8</sup> A. R. West, *Basic Solid State Chemistry*, ISBN: 0-471-98755-7, JOHN WILE & SONS, NEW YORK (1991).
- <sup>9</sup> W. G. Cady, *PIEZOELECTRICITY*, Dover Publications, Inc (1964).
- <sup>10</sup> Uchino, K. *Ferroelectric Devices* (Marcel Dekker, New York, 2000).
- <sup>11</sup> B. Jeff, *et al*, *Piezoelectric Ceramics*, Academic Press, London (1971).
- <sup>12</sup> S. E. Park and T. R. Shrout, *J. Appl. Phys.* 82, 1804 (1997)
- <sup>13</sup> N, noheda, *et al* , *Phase Transitions* 79, 5 (2006)
- <sup>14</sup> J. Wang, J. B. Neaton, H. Zheng et al., *Science* **299**, 1719 (2003)
- <sup>15</sup> Nagarajan, V. et al, *Appl. Phys. Lett.* 81, 4215-4217 (2002).
- <sup>16</sup> W. Eerenstein *et al.* *Science*, 307, 1203a (2005).

- 
- <sup>17</sup> S. Fujino *et al*, *Solid. State Ionics*, 178, 1257 (2007)
- <sup>18</sup> T. Kimura, T. Goto, H. Shintani, K. Ishizaka, T. Arima, and Y. Tokura, *Nature (London)* **426**, 55-58 (2003).
- <sup>19</sup> M. Fiebig, Th. Lottermoser, D. Fröhlich, A. V. Goltsev, and R. V. Pisarev, *Nature (London)* **419**, 818-820 (2002).
- <sup>20</sup> G. A. Smolenskii and I. Chupis, *Sov. Phys. Usp.* **25**, 475 (1982).
- <sup>21</sup> J. Wang, J. B. Neaton, H. Zheng, V. Nagarajan, S. B. Ogale, B. Liu, D. Viehland, V. Vaithyanathan, D. G. Schlom, U. V. Waghmare, N. A. Spaldin, K. M. Rabe, M. Wuttig, and R. Ramesh, *Science* **299**, 1719-1722 (2003).
- <sup>22</sup> J. B. Newton *et al*, *Phys. Rev. B* 71, 014113 (2005).
- <sup>23</sup> M. Mahesh Kumar, V. R. Palkar, K. Srinivas, S. V. Suyanarayana, *Appl. Phys. Lett.* 76, 2764 (2000)
- <sup>24</sup> M. Murakami, S. Fujino, S.-H. Lim, L. G. Salamanca-Riba, M. Wuttig, I. Takeuchi, H. Sugaya, T. Hasegawa, and S. E. Lodland, *Appl. Phys. Lett.*, 88, 112505, (2006)
- <sup>25</sup> X. Qi, J. Dho, R. Tomov, M. G. Blamire, and J. L. MacManus-Driscoll, *Appl. Phys. Lett.*, 86, 062903, (2005)
- <sup>26</sup> G. W. Pabst, L. W. Martin, Y.-H. Chu, and R. Ramesh, *Appl. Phys. Lett.*, 90, 072902 (2007)
- <sup>27</sup> J. R. Teague, R. Gerson, and W. J. James, *Solid State Commun.* 8, 1073 (1970)
- <sup>28</sup> W. Eerenstein, F. D. Morrison, J. Dho, M. G. Blamire, J. F. Scott, and N. D. Mathur, *Science* **307**, 1203a (2005)

- 
- <sup>29</sup>J. Wang, A. Scholl, H. Zheng, S. B. Ogale, D. Viehland, D. G. Schlom, N. A. Spaldin, K. M. Rabe, M. Wuttig, L. Mohaddes, J. Neaton, U. Waghmare, T. Zhao, and R. Ramesh, *Science* **307**, 1203b (2005)
- <sup>30</sup>H. Béa, M Bibes, A. Barthélémy, K. Bouzehouane, E. Jacquet, A. Khodan, J.-P. Contour, S. Wyczisk, A. Forget, D. Lebeugle, D. Colson, and M. Viert, *Appl. Phys. Lett.* **87**, 072508 (2005)
- <sup>31</sup> Chemical & engineering NEWS, August (2001)
- <sup>32</sup> J. Wang *et. Al*, *Science*, vol 179, 1712 (1996)
- <sup>33</sup> H. Koinuma and I Takeuchi, *Nature material*, vol 3, 429 (2004)
- <sup>34</sup> K. S. Chang, M. A. Aronova, C.-L. Lin, M. Murakami, M.-H. Yu, J. Hattrick Simpers, O. O. Famodu, S. Y. Lee, R. Ramesh, M. Wuttig, I. Takeuchi, C. Gao, and L. A. Bendersky, *Appl. Phys. Lett.* **79**, 4411 (2001)
- <sup>35</sup> Bulker (XRD equipment) : <http://www.bruker-axs.de/microanalysis.html>
- <sup>36</sup> B. B. He, U. Preckwinkle, and K. L. Smith, *International Center for Diffraction Data, Advances in X-ray Analysis*, 46, 37 (2003)
- <sup>37</sup> D. B. Williams and C. B. Cater, *Transmission Electron microscopy*, ISBN: 0-306-4524-2, Plenum Press, New York (1996)
- <sup>38</sup> S.-H. Lim thesis (Unpublished)
- <sup>39</sup> W. KÄNZIG, *Ferroelectrics and Antiferroelectrics*, Academic Press, New York and London(1957)
- <sup>40</sup> K. Rabe, C. H. Ahn, and J. -H. Triscone (Eds.), *Physics of Ferroelectrics*, ISBN 978-3-540-34590-9, Springer Berlin Heidelberg New York (2007)
- <sup>41</sup> S. O. Kasap, *Electronic Materials and devices*, ISBN 0-07-295791-3,

- 
- <sup>42</sup> M. Murakami, S. Fujino, S.-H. Lim, *et al*, Appl. Phys. Lett, 88, 112505 (2006)
- <sup>43</sup> M. Murakami, S. Fujino, S.-H. Lim, *et al*, Appl. Phys. Lett, 88, 152902 (2006)
- <sup>44</sup> S. Fujino, M. Murakami, S.-H. Lim, *et al*, J. Appl. Phys, 101, 013903 (2007)
- <sup>45</sup> T. Kanai, S. Ohkoshi, and K. Hashimoto, J. Phys. Chem.Solids 64, 391 (2003)
- <sup>46</sup> S.Y.Yang, F.Zavaliche, L. Mohaddes-Ardabili, V. Vaithyanathan, D. G. Schlom, Y. J. Lee, Y. H. Chu, M. P. Cruz, Q. Zhan, T. Zhao, and R. Ramesh, Appl. Phys. Lett, 87, 102903 (2005)
- <sup>47</sup> S.-H. Lim, *et al* , *Adv. Funct. Mater.* 17, 2594 (2007)
- <sup>48</sup> K. Y. Young, M. Noda, and K. Okuyama, Appl. Phys. Lett, 83, 3981, (2003)
- <sup>49</sup> Y. P. Wang, L. Zhou, M. F. Zhang, X. Y. Chen, J-M, and Z. G. Liu,  
Appl. Phys. Lett, 84, 1731, (2004)
- <sup>50</sup> J. Dho, X. Qi, H. Kim, J. MacManus-Driscoll, and M. G. Blamire, *Adv. Mater*, 18, 1445 – 1448, (2006)
- <sup>51</sup> J. R. Cheng and L. E. Cross, J.Appl. Phys. 94, 5188, (2003)
- <sup>52</sup> G. L. Yuan *et al.* J. Appl. Phys. 101, 024106 (2007)
- <sup>53</sup> S. Fujino, M. Murakami, V. Nagarajan, S.-H. Lim, A. Varatharajan, C. Fennie,  
M. Wuttig, L. G.. Salamanca-Riba, and I. Takeuchi, Accepted Appl. Phys. Lett,  
(2008)
- <sup>54</sup> J-K. Kim, S-S. Kim, W-J. Kim, A.S. Bahalla, and R.Guo,  
Appl. Phys. Lett, 88, 132901, (2006)
- <sup>55</sup> S. K. Singh, Y. K. Kim, H. Funakubo, and H. Ishiwara,  
Appl. Phys. Lett, 88, 132901, (2006)
- <sup>56</sup> S. K. Singh, H. Ishikawa, and K. Maruyama, Appl. Phys. Lett, 88, 262908, (2006)

- 
- <sup>57</sup> J. Wang, J. B. Neaton, H. Zheng et al., *Science* **299**, 1719 (2003)
- <sup>58</sup> Y. Saito, H. Takao, T. Tani et al., *Nature* **432**, 84 (2004)
- <sup>59</sup> H. Uchida, R. Ueno, H. Funakubo et al., *J. Appl. Phys.* **100**, 014106 (2006).
- <sup>60</sup> G. L. Yuan, S. W. Or, J. M. Liu et al., *Appl. Phys. Lett.* **89** (5), 052905 (2006)
- <sup>61</sup> G. L. Yuan and S. W. Or, *J. Appl. Phys.* **100**, 024109 (2006).
- <sup>62</sup> S. E. Park and T. R. Shrotr, *J. Appl. Phys.* **82**, 1804 (1997).
- <sup>63</sup> R. Guo, L. E. Cross, S. -E. Park et al., *Phys. Rev. Lett.* **84**, 5423 (1999).
- <sup>64</sup> D. E. Cox, B. Noheda, G. Shirane et al, *Appl. Phys. Lett.* **79**, 400 (2001).
- <sup>65</sup> M. R. Suchomel and P. K. Davies, *J. Appl. Phys.* **96**, 4405 (2004).
- <sup>66</sup> I. Grinberg, M. R. Suchomel, P. K. Davies et al., *J. Appl. Phys.* **98**, 094111 (2005).
- <sup>67</sup> Jona, F. & Shirane, G. *Ferroelectric Crystals* (Pergamon, New York, 1962).
- <sup>68</sup> Zhang, S. T. *et al*, *Appl. Phys. Lett.* **88**, 162901 (2006).
- <sup>69</sup> Suchomel, M. R. & Davies, P. K, *J. Appl. Phys.* **96**, 4405-4410 (2004).
- <sup>70</sup> Grinberg, I., Suchomel, M. R., Davies, P. K. & Rappe, A. M,  
*J. Appl. Phys.* **98**, 094111 (2005).
- <sup>71</sup> Fu, H. X. & Cohen, R. E, *Nature* **403**, 281-283 (2000).
- <sup>72</sup> Vanderbilt, D. & Cohen, M. H, *Phys. Rev. B* **63**, 094108 (2001).
- <sup>73</sup> Noheda, B. *et al*, *Phys. Rev. B* **63**, 014103 (2001).
- <sup>74</sup> Nagarajan, V. *et al*, *Appl. Phys. Lett.* **81**, 4215-4217 (2002).
- <sup>75</sup> Trolrier-McKinstry, S., Gharb, N. B. & Damjanovic, D,  
*Applied Physics Letters* **88** (2006).
- <sup>76</sup> Nagarajan, V. *et al*, *Appl. Phys. Lett.* **81**, 4215-4217 (2002).
- <sup>77</sup> Ravindran, P., Vidya, R., Kjekshus, A., Fjellvag, H. & Eriksson, O,

- 
- Phys. Rev. B 74 (2006).
- <sup>78</sup> Jaffe, B., Cook, W. R. & Jaffe, H. Piezoelectric Ceramics  
(Academic press, London (1971).
- <sup>79</sup> CITIZEN, How long can you wait for a starting up PC ?,  
[http://www.citizen.co.jp/research/time/20030528/01\\_03.html](http://www.citizen.co.jp/research/time/20030528/01_03.html)
- <sup>80</sup> D. Kahng and S.M. Sze, The Bell System Technical Journal, vol. 46, no. 4, 1288  
(1967)
- <sup>81</sup> OVONYX :PRAM : <http://ovonyx.com/technology/technical-presentation.html>
- <sup>82</sup> Fujitsu Technology report:  
[http://www.fujitsu.com/downloads/MICRO/fma/pdf/framppt\\_tech.pdf](http://www.fujitsu.com/downloads/MICRO/fma/pdf/framppt_tech.pdf)
- <sup>83</sup> IBM Technology report:  
<http://www.research.ibm.com/journal/rd/255/ibmrd2505V.pdf>
- <sup>84</sup> A. Chaiken, *et al*, Appl. Phys. Lett, 59, 240,(1991)
- <sup>85</sup> Ch. Bink and D. Doubin, J. Phys. Condens. Matter, 17, 39 (2005)
- <sup>86</sup> S.-H. Lim *et,al* (*unpublished*)
- <sup>87</sup> M. Fiebig, J. Phys. D: Appl. Phys. 38123 (2005)
- <sup>88</sup> H. N. Al-Shareef, *et al*, Appl. Phys. Lett, 68, 690 (1996)
- <sup>89</sup> R. Ramesh *et al*, Material Science and Engineering, 32, 191 (2001)
- <sup>90</sup> Fujitsu: Mn doped BiFeO for FeRAM:  
[http://www.fujitsu.com/us/news/pr/fma\\_20060802.html](http://www.fujitsu.com/us/news/pr/fma_20060802.html)